Fuel 362 (2024) 130713

Contents lists available at ScienceDirect

Fuel

journal homepage: www.elsevier.com/locate/fuel

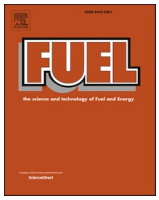

Full Length Article

Experimental and simulation studies of oxygen-blown, steam-injected, entrained flow gasification of lignin

Nastaran Samani [a,*], Roger Khalil [b], Morten Seljeskog [b], Jørn Bakken [b], Rajan K. Thapa [a], Marianne S. Eikeland [a]

[a] University of South-Eastern Norway, Porsgrunn, Norway
[b] SINTEF Energy Research, Trondheim, Norway

ARTICLE INFO

Keywords:
Entrained Flow Reactor
Eulerian-Lagrangian Simulation
Biomass gasification
Cold Gas Efficiency
Lignin

ABSTRACT

This article presents results from experimental and simulation studies on a laboratory-scale pressurized O_2-blown Entrained Flow biomass gasification Reactor (EFR) using pulverized commercial lignin pellets as feedstock. The primary focus lies in the assessment of the EFR's performance indicators such as the H_2/CO ratio, the Cold Gas Efficiency (CGE), and the Carbon Conversion Efficiency (CCE). The gasifier was operated at an absolute pressure of 8.2 bars, with varying amounts of O_2 and steam. In the first series of experiments, the O_2 equivalence ratio varied between 0.2 and 0.8, with no steam injection. This yielded a maximum CGE of 47%, a CCE of 94%, and an H_2/CO ratio within the range of 0.4–0.7. In the last series of experiments, a perforated horizontal steam tube was installed allowing for a variation of the steam-to-biomass ratio (S/B), between 0.5 and 1.5. At a S/B of 1.5, the CGE and the CCE were at their highest levels of 91% and 99%, respectively. Based on the experimental setup, a 3D multiscale Eulerian-Lagrangian computational particle fluid dynamics (CPFD) model for the reactor was developed and validated against the experimental data. This model was then employed to explore the impacts of reactor temperature, S/B, equivalence ratio (λ), and the lignin particle size distribution (PSD) on the gasification process. The findings show that increased reactor temperature enhances H_2 and CO production. Higher S/B ratios lead to greater H_2 production but reduced CO production. Increased S/B ratios improve both CGE and CCE. Larger particles and higher λ values decrease CO and H_2 production. Without steam injection, the peak CGE occurs at $\lambda \approx 0.45$, corresponding to complete CH_4 conversion. Beyond this point, as λ increases, reactor temperatures rise while CGEs decrease. Simulations reveal the optimal λ range for steam injection is 0.15–0.35. A sensitivity analysis highlights the significant impact of reactor temperature on H_2 and CO production. While λ shows high sensitivity for H_2 production, the S/B ratio exerts a greater impact on CO production.

1. Introduction

Over the past few decades, a reexamination of renewable energy resources has been prompted by several factors that are cause for concern. These factors include the acceleration of global warming, the depletion of fossil reserves, and the growing global demand for energy [1,2]. Energy production using fossil fuels harms society, politics, and the environment. The combustion of fossil fuels has increased the global concentration of CO_2 in the atmosphere and exacerbated climate change. Biomass, one of the most promising renewable resources, has attracted more attention as it is the world's fourth-largest energy resource after coal, oil, and natural gas. In Norway, significant forest residues and waste wood from households and industrial activities are generated yearly, making them potential sources for renewable energy production. Specifically, forest residues amount to about 3.7 million m^3 yearly, while waste wood has an annual generation of 800,000 tons or about 2.6 million m^3/y [3]. To meet the country's ambition of increased renewable energy production, it is important to explore efficient ways of using the available biomass.

The transformation of biomass into useful products can be done through a variety of processes, including thermal conversion, thermochemical conversion, biochemical conversion, and chemical conversion, amongst others. The term "gasification" refers to the thermochemical conversion of a carbon-based solid fuel into a synthesis gas in the

* Corresponding author.
E-mail addresses: nastaran.samani@usn.no (N. Samani), roger.a.khalil@sintef.no (R. Khalil), morten.seljeskog@sintef.no (M. Seljeskog), jorn.bakken@sintef.no (J. Bakken), rajan.k.thapa@usn.no (R.K. Thapa), marianne.eikeland@usn.no (M.S. Eikeland).

https://doi.org/10.1016/j.fuel.2023.130713
Received 28 July 2023; Received in revised form 7 December 2023; Accepted 20 December 2023
Available online 4 January 2024

presence of various mediums, such as air, oxygen, water, carbon dioxide, and hydrogen [4,5]. It is a chemical process that consists of many overlapping reactions in the gas and solid phases. These reactions depend on the process parameters (temperature and pressure), the properties of the fuel, the gasification agents, and the stoichiometry of the mixture [6]. The process of gasification results in the production of synthesis gas and ash or slag (mineral residues). The gas primarily consists of carbon monoxide and hydrogen, along with minute amounts of light hydrocarbons, carbon dioxide, and nitrogen [7,8]. Converting a solid feedstock into a gas fuel through gasification is an effective method for improving the quality of the feedstock [9]. The gasifiers can be categorized into three major groups: fixed bed, fluidized bed, and entrained flow reactors [10]. Although the EFR is a well-known technology for coal gasification, it is not yet capable of being run with biomass as feedstock and hence requires further development. The high conversion of biomass into syngas with a low tar content, which is ideal for biofuel synthesis processes, is the primary benefit of this technique [11]. Previous studies have shown that tars were present at low gasification temperatures, while high temperatures produced significant soot and almost no tars [12]. The advantages of EFRs include high operating pressure, high gasification temperature, and short residence time, allowing for the design of compact reactors [13,14]. Experimental research and modeling have both been used to advance our understanding of this technology. Experimentation is typically carried out in lab-scale reactors, which enable the reproduction of key EFR features such as temperature, heat flow, residence time, and particle size. Zhou et al. [15] investigated the properties of three types of biomass: rice husk, sawdust, and camphor wood gasification carried out in a bench-scale laminar entrained flow gasifier. Experiments were carried out to explore the influence of important parameters, such as reaction temperature, residence time, and oxygen/biomass ratio. They found out that the production of H_2 and CO was boosted with the increase in temperature. Increasing the residence time resulted in a higher rate of carbon conversion and an improvement in the syngas quality. Qin et al. [12] studied the gasification of wood and straw, in a laboratory-scale atmospheric entrained flow reactor. The effects of the reaction temperature, the steam/carbon molar ratio, the surplus air ratio, and biomass type were explored on the solid, liquid, and gas products. To achieve full conversion within the hot temperature zone, a fuel that has been mechanically processed down to powdery-sized particles is necessary due to the short residence times. Several parameters were investigated to optimize the gasification process of wood powder in an oxygen-blown entrained flow gasifier, including equivalence ratio, oxidant type (air or oxygen), thermal load, pressure, and particle size distribution (PSD) of the wood powder by Weiland et al. [16,17]. The influences of H_2O, CO_2, and O_2 addition on biomass gasification were experimentally studied in a drop tube reactor, and modeled using a 1-D model (GASPAR) by Billaud et al. [18]. They found that at temperatures of 800 and 1000 °C, adding water or carbon dioxide does not affect the gasification product yields. However, at temperatures of 1200 and 1400 °C, the char gasification is significantly enhanced, and the formation of soot is inhibited. Liao et al. [19] experimentally explored entrained flow gasification of raw and torrefied pine sawdust (PS) at a temperature of 1300 °C with varying equivalency ratios (ERs). Both the impact of torrefaction conditions and the relationship between the amount of soot produced and the volatile content of the feedstock on the gasification performance were explored. According to their findings, PS that had been torrefied at 280 °C performed significantly better than raw PS. In addition, they discovered that the torrefaction pretreatment decreased the amount of soot produced.

Given there is a limit to both the time and money for experimentation, simulations are a low-cost method for investigating the potential benefits, costs, and risks associated with the implementation of gasification. The field of multiphase reacting flows benefits greatly from computational fluid dynamics (CFD) models for their predictive capacity. All the existing CFD models can be roughly classified into either the Eulerian-Eulerian or the Eulerian-Lagrangian categories. Both the fluid and particle phases are viewed as interpenetrating continua in the Eulerian-Eulerian method. However, the Eulerian-Eulerian approach has issues modeling flows with a variety of particle types and sizes because it does not identify the discrete character of the particle phase and hence cannot provide closure models for interphase interaction within its continuous framework. One of the significant drawbacks of the Eulerian-Eulerian approach is its fundamental assumption of continuum behavior for both the fluid and solid phases. In a multiphase system, particularly when solid biomass feedstock is being converted into syngas, this simplifying assumption may not adequately capture the intricate interactions between the gas and solid particles. For example, a comparison of simulation results obtained through the Eulerian-Eulerian method with available experimental data revealed substantial disparities, especially with a riser featuring a solids side inlet [20]. The disparities were significantly mitigated when employing the Eulerian-Lagrangian method, as shown in this study [21]. By taking an Eulerian-Lagrangian approach, in which the gas phase is represented as a continuous fluid where cells and particles are modeled as discrete Lagrangian points, it is possible to naturally get around the challenges presented here. By directly integrating the equations of motion while considering interactions with the continuous phase, each particle's position and trajectory in space and time may be determined [21]. Adeyemi et al. [22] applied the Eulerian-Lagrangian approach to study the entrained flow gasification of two feedstocks, Kentucky coal, and woody biomass. They carried out some experimental tests in the air-blown atmospheric drop tube reactor facility to confirm the model. They investigated the influence of feedstock type on the composition of the gas produced along the centerline of the gasifier and found that Kentucky coal achieved a better gasification efficiency than wood waste. Timsina et al [23] have developed a three-dimensional CPFD model to simulate an entrained flow (EF) gasification reactor. The model was validated against an experiment published in the literature. Ku et al [24] developed a multiscale Eulerian − Lagrangian CFD model to investigate the effects of the operating condition and reactor structure on the biomass EFR. They studied the effects of three parameters on the gasification process including the gasifying agent, the reactor structure, and the fuel properties. They found that oxygen can improve the production of CO and CCE compared to other gasifying mediums. However, the excessive resulted in a decline in combustible gas yield and CGE. Throughout the past decade, simulations of coal combustion or gasification have increasingly made use of an Eulerian-Lagrangian approach [25–27]. However, due to issues with slagging, and costly experiments, there is a severe lack of experimental gasification data.

Lignin, the second most abundant natural polymer, makes up a significant part of biomass, typically comprising 20–30 % of woody biomass. It is rich in carbon content, making it a potential energy source. Lignin is often a byproduct of chemical pulping [28] and is burned to recover chemicals and produce steam. It is also generated during ethanol production from lignocellulosic biomass and can be gasified to create fuel gas and valuable products [29]. Furusawa et al. [30] experimentally investigated the generation of hydrogen through the gasification of lignin, using Ni/MgO catalysts in supercritical water, within a stainless steel tube bomb reactor. Öhrman et al. [31] conducted experimental tests on lignin residue obtained from the biochemical conversion of wheat straw, subjecting it to gasification in a pressurized EF gasifier (PEBG). The gasification process operated at a thermal power range of 0.25–0.30 MWth, using an oxygen-blown method and maintaining a lambda (λ) range between 0.45 and 0.5, all under a pressure of 1 bar (g). Zhou et al. [32] investigated the influence of various reaction parameters, including temperature, heating rate, and reaction atmosphere, on the generation of polycyclic aromatic hydrocarbons from lignin in a fixed-bed reactor. Liakakou et al. [33] experimentally discussed the use of lignin-rich residues derived from second-generation bioethanol production to generate syngas suitable for gas fermentation. The research explores three gasification technologies, each operating at a distinct

scale: fixed bed updraft gasification (30 kg/h solid feed), bubbling fluidized bed gasification (0.3 kg/h solid feed), and indirect gasification (3 kg/h solid feed). Two lignin-rich residues with varying properties were tested, with a focus on assessing the impact of feedstock pretreatment (including grinding, drying, and pelleting) and the syngas quality requirements for the fermentation process. Lu et al. [34] used the MFiX CFD software to develop and confirm a detailed biomass pyrolysis kinetics model. The study showed that bio-char yield was significantly influenced by carbon-rich lignin and tannin pseudo-species, while bio-oil and bio-gas yields were linked to oxygen-rich lignin pseudo-species. Chen et al. [35] created a CFD model that distinguishes soot precursors, such as cellulose, hemicellulose, and lignin, within a component-based pyrolysis framework. The model's validity was confirmed through pyrolysis experiments, and it was used to investigate soot formation during biomass steam gasification across various temperature and S/B conditions.

In this study, an Eulerian-Lagrangian model was developed for the EF gasification of lignin. All heat and mass transfer, pyrolysis, homogeneous and heterogeneous reactions, radiation, and interactions between the continuous gas phase and discrete particles have been implemented. The impacts of the operating parameters reactor temperature, steam/biomass ratio, equivalence ratio (λ), and biomass size distribution on the syngas generation and composition were studied. The model was also confirmed by running gasification experiments with lignin powder in a laboratory-scale EFR (10–20 kW). The goal of this paper is to bridge the existing knowledge gap by investigating the impact of various operating conditions on the process temperature, syngas yield, carbon conversion, and process efficiency in the context of EF gasification of biomass. In addition, lignin, being one of the most common organic materials, is experimentally tested as feedstock. The paper explores how different parameters, including (i) reactor temperature, (ii) steam-to-biomass ratio, (iii) the equivalence ratio, and (iv) the biomass particle size, influence gas composition within typical ranges. This study provides further insight into the EF gasification of lignin, which can help upscale the technology for sustainable biofuel production processes.

2. Material and experimental methods

2.1. Lignin

Lignin, a complex three-dimensional polymer found in plant cell walls, is the second most abundant organic material on Earth, following cellulose. Its intricate structure and composition make it challenging to convert into useful products. However, there is growing interest in extracting lignin efficiently from biomass for the production of high-value chemicals and materials, including biofuels, bioplastics, and carbon fiber. One promising approach is hydrothermal conversion, encompassing methods like hydrothermal gasification, wet oxidation, and hydrothermal liquefaction. These processes can yield fuel gas, aromatic aldehydes, and phenolic products [36]. Lignin gasification offers advantages over other biomass conversion methods like combustion and pyrolysis. It produces cleaner-burning fuel, has higher energy conversion rates, and offers better control and consistency, making it suitable for integration into existing energy systems [37]. The lignin used in this study was sourced from the Finnish company St1 lignocellulosic ethanol Cellunolix production process. The proximate and ultimate analyses of the lignin used in experimental tests are summarized in Table 1. The PSD of lignin feedstock is shown in Fig. 1. The measurement of PSD was performed in a Mastersizer 3000 [38], an optical instrument that measures particles suspended in gas or liquid. The data shown below are based on dry measurements which have been more reliable for biomass particles.

2.2. Experimental setup and data

The EFR is built up with many of the sub-systems found in a full-scale gasification plant and is designed for a fuel feed between 10 and 20 kW, allowing for detailed studies at a small-scale. The reactor itself and the subsequent coolers were all designed for a maximum of 10 bar(a) operating pressure. The cooling system consists of two sub-systems, a radiative cooler followed by a convective cooler with a combined cooling capacity of about 60 kW [39]. After syngas cooling, propane is mixed in, before the gas mixture is combusted in a gas burner, after which the flue gas is ejected over the roof.

A schematic illustration of the EFR along with all its sub-systems, as well as the physical layout and sizing of the reactor and hopper, are shown in Fig. 2. The inner diameter of the reactor volume is 200 mm and has a height of 800 mm.

The slag/ash/unconverted materials are collected in a container at the bottom outlet after the main cooler. All thermocouples are situated inside the refractory and do not penetrate the inner core wall. TC16 (see Fig. 2a) regulates the reactor core temperature according to a predefined setpoint by adjusting the electrical power, provided by a 40-kW transformer, to the heating elements. TC14 is used for overheating monitoring and TC33-35 can be installed to verify the reactor core temperature. Before conducting the experiments, the temperature inside the reactor core was measured and compared to the set point temperature. Three thermocouples were installed along the length of the reactor, as illustrated by the positions in Fig. 2b, to monitor temperature variations in response to thermal input. The thermocouples displayed good temperature stability, with temperatures varying within −50 °C of the set point. Six electrically heated elements, type Kanthal Super 1700 918, Lu '440′, are circumferentially distributed inside the refractory lining to preheat and control the reactor core gas volume to the reactor setpoint temperature before the start of an experiment and maintain this during gasification. The reactor was preheated at 100 °C/h overnight to the reactor setpoint temperature. The oxidant, used was industry quality O_2, supplied from standard pressurized cylinders. During the experiments, several input variables were kept constant, i.e., feedstock rate/power (2 kg/h or 11.5 kW), reactor pressure (8.2 bar(a)), and temperature (1150 °C), as well as the N_2 stream for feedstock transport (60.2 Nl/min), with corresponding variances of, $s^2 = 0.52/0.01$, 0.07, 120.1 and 1.72. Then a variation in the experimental series was run, where the O_2 stream to the burner was varied (6.1–26.2 Nl/min) in steps to obtain a variation in the air-to-fuel ratio between 0.18 and 0.82. Mass flow controllers were employed to precisely regulate the flow rates of various agents. Continuous lignin feed into the reactor was achieved via a loss-in-weight-based screw feeding system, seamlessly delivering biomass particles from a sealed 50-liter fuel storage hopper to the reactor's uppermost burner head. This configuration allowed for approximately 8 h of uninterrupted operation. To analyze syngas composition, a Varian CP-4900 micro-gas chromatograph (GC) equipped with two distinct columns was utilized. The first column, a 10-meter Pora-plot type with an inner diameter of 0.25 mm, employed high-purity Helium 6.0 as the carrier gas. This column effectively separated CO_2, CH_4, $C_2H_2 + C_2H_4$, and C_2H_6. The second column, a 10-meter Molsieve with an inner

Table 1
Biomass properties for lignin.

Proximate analysis (wt.%, wet basis)				Ultimate analysis (wt.%, dry basis)						HHV (MJ/kg)
Moisture	Volatile	Fixed carbon	Ash	C	H	N	O	S	ash	
8.2	65.8	25.68	0.32	54.8	6.3	0.78	37.69	0.11	0.3	23.512

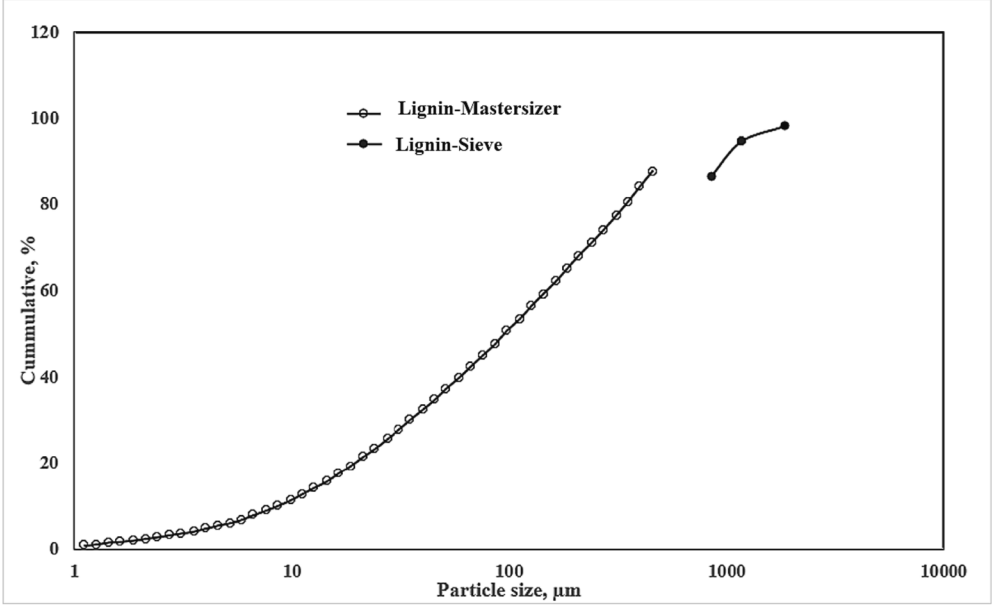

Fig. 1. PSD for lignin particles.

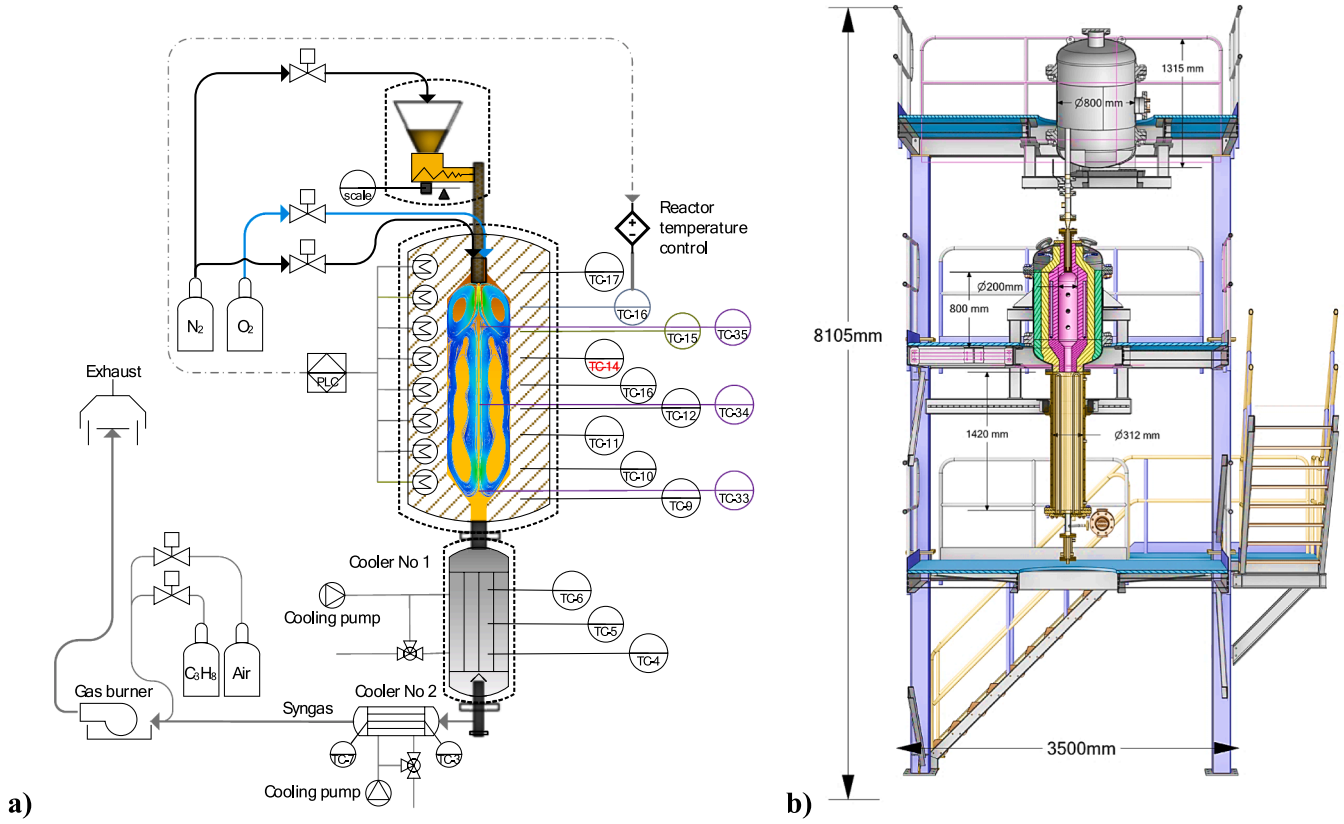

Fig. 2. a) The ER reactor and its sub-systems b) The EFR is built into a frame for easy access to the hopper and for the reactor for cleaning and maintenance.

diameter of 0.25 mm, utilized Argon 6.0 as the carrier gas. This choice of Argon over Helium enabled the detection of H_2. The second column facilitated the separation of H_2, O_2, N_2, CH_4, and CO. Prior to each measurement campaign, the GC was calibrated using a calibration cylinder containing precise concentrations of all target compounds. This calibration gas cylinder, acquired from AGA, offered an uncertainty of ± 2 % for all compounds contained within it. Experiments #1–5 were carried out with different values λ and pure oxygen supplied through the burner head. In Exp #6–9, extra N_2 was added to the burner (3–21.4 Nl/min) either to increase or keep the burner head velocity constant, while reducing the O_2 stream. Exp #10–13 were run with an increasing S/B (0.5–1.5) while reducing the O_2 stream to the burner. The steam was injected through a perforated transversal tube as shown in Fig. 3a, with 7x2 Ø1 mm injection ports, angled 20° upwards. The burner head is

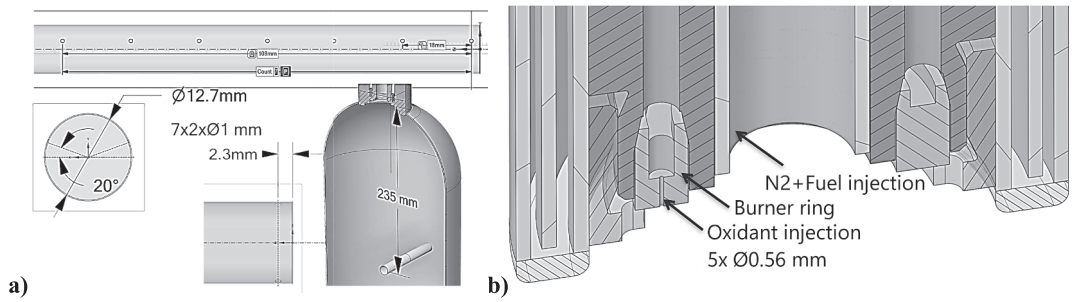

Fig. 3. A) the water-cooled burner head with an exchangeable burner ring. b) steam injection tube situated in the reactor core center, 7x2x ø1mm injection holes, angled 20° upwards.

shown in Fig. 3b, with a central feedstock injection and its circumferential oxidant injection ports and the so-called burner ring. The current burner head configuration and reactor pressure resulted in velocities between 10.7 and 52.5 m/s. It is important to highlight that the temperature conditions during the lignin experiments did not result in any slagging problems.

The results from the gasification of lignin are given in Table 2, by syngas composition (vol%) and production (Nl/min), with varying amounts of oxidant and steam. Corresponding values for syngas composition, CGE, and CCE are discussed in section 5. Regarding the determination of the residence time within the reactor, it was calculated as the ratio of the dry gas volume flow over the reactor volume, thus providing a mean residence time. The syngas volume flow was determined based on the measured N_2 concentration obtained from the GC and the known quantity of nitrogen supplied through the mass flow controllers, assuming that the nitrogen (N_2) remained inert and that any contribution from N_2 within the lignin was disregarded.

3. Computational method

3.1. The CPFD method

The Barracuda Virtual Reactor uses a numerical scheme found in the Eulerian-Lagrangian model to simulate a large-scale multiphase (particle–fluid) flow system in three dimensions. The CPFD methodology incorporates the multiphase particle-in-cell (MP-PIC) method and the particle parceling algorithm to solve the gas phase as a continuous fluid in an Eulerian grid of cells where particles are modeled as discrete Lagrangian points [40,41].

3.2. Continuous gas phase

The volume-averaged Navier-Stokes equation is used to describe the continuous gas phase when the frame of reference is Eulerian. The equations for the conservation of mass and momentum in the gas phase are [42]:

$$\frac{\partial(\theta_g\rho_g)}{\partial t}+\nabla.(\theta_g\rho_g\boldsymbol{u}_g)=\delta\dot{m}_p \tag{1}$$

$$\frac{\partial(\theta_g\rho_g\boldsymbol{u}_g)}{\partial t}+\nabla.(\theta_g\rho_g\boldsymbol{u}_g\boldsymbol{u}_g)=\nabla.(\theta_g\tau_g)+\boldsymbol{F}+\theta_g\rho_g\boldsymbol{g}-\nabla p \tag{2}$$

Where θ_g, ρ_g and $\boldsymbol{u}_g$ are the volume fraction, density, and velocity of the gas phase, respectively. $\delta\dot{m}_p$ represents the rate of mass production of gas per volume from gas-particle reactions. p is the mean flow gas thermodynamics pressure, $\boldsymbol{g}$ is the gravitational acceleration, and $\boldsymbol{F}$ is the interphase momentum transfer rate per volume.τ_g represents the non-hydrostatic part of the gas stress tensor and is given by equation 3.

$$\tau_g=\mu\left(\nabla\boldsymbol{u}_g+\nabla\boldsymbol{u}_g^T\right)-\frac{2}{3}\mu_g I(\nabla.\boldsymbol{u}_g) \tag{3}$$

$$\mu_g=\mu_l+\mu_t \tag{4}$$

Where μ is a shear viscosity and according to the Smagorinsky [43] turbulence model, it is the sum of the laminar μ_l and turbulence viscosity μ_t. Large eddy simulation, which directly resolves large-scale gas motions and models subgrid scales using the Smagorinsky model [43], is used to successfully resolve the turbulence in the system. To calculate large eddies and unresolved subgrid turbulence, eddy-viscosity can be applied.

$$\mu_t=C\rho_g\Delta^2\sqrt{\left(\nabla\boldsymbol{u}_g+\nabla\boldsymbol{u}_g^T\right)^2},\Delta=\sqrt[3]{\Delta x\Delta y\Delta z} \tag{5}$$

Where C is the Smagorinsky coefficient used in the gasifier calculations and is C = 0.01. Δ is the subgrid length scale used in the three orthogonal spheres whose dimensions are determined by taking the cube root of the product of the filtered length along x, y, and z directions (i.e., Δx,Δy,Δz).

To determine the overall properties of the fluid, a transport equation must first be solved for each individual gas species.

Table 2
The experimental tests from the gasification of lignin with varying amounts of oxidant and steam.

Exp.	λ	Residence time (s)	S/B	CH_4 (%)	CO_2 (%)	H_2 (%)	CO (%)	H_2/CO	Syngas (NL/min)	CGE (%)	CCE (%)
Exp. 1	0.7	24	–	1.4	47.3	16.7	34.6	0.5	91	32 %	89 %
Exp. 2	0.8	24.1	–	0.8	57.7	12.6	28.9	0.4	92	25 %	93 %
Exp. 3	0.6	23.5	–	2.3	39	18.9	39.6	0.5	93	41 %	92 %
Exp. 4	0.7	21.7	–	1.4	39	19.4	40.2	0.5	102	40 %	94 %
Exp. 5	0.5	21.4	–	2.4	32.4	21.8	43.3	0.5	103	46 %	93 %
Exp. 6	0.4	24.4	–	4.8	28.3	25.4	41.1	0.6	94	38 %	62 %
Exp. 7	0.4	22.6	–	4.7	28.7	25.2	41	0.6	109	39 %	66 %
Exp. 8	0.4	24.1	–	4.5	26.3	25.9	43	0.6	95	41 %	66 %
Exp. 9	0.2	22.9	–	8	18.2	29.6	43.7	0.7	100	47 %	60 %
Exp. 10	0.4	21.2	0.5	3.9	26.3	35	34.6	1	104	64 %	93 %
Exp. 11	0.4	19.3	1	2.6	26.3	41.5	29.5	1.4	114	74 %	99 %
Exp. 12	0.4	18.5	1.5	2.7	28.2	43.9	25.2	1.7	118	79 %	101 %
Exp. 13	0.2	18.2	1.5	3.7	22.5	48.7	25	1.9	121	91 %	99 %

$$\frac{\partial(\theta_g\rho_g x_{g,i})}{\partial t} = \nabla.(\theta_g\rho_g x_{g,i}\boldsymbol{u}_g) = \nabla.(\theta_g\rho_g D\nabla x_{g,i}) + \delta\dot{m}_{i,chem} \tag{6}$$

Where $x_{g,i}$ is the mass fraction of gas species and D is the turbulent mass diffusivity. $\delta\dot{m}_{i,chem}$ is defined as the chemical source term.

The energy equation of the gas phase is given by,

$$\frac{\partial}{\partial t}(\theta_g\rho_g h_g) + \nabla.(\theta_g\rho_g h_g\boldsymbol{u}_g) = \theta_g\left(\frac{\partial p}{\partial t} + \boldsymbol{u}_g.\nabla p\right) + \phi - \nabla.(\theta_g\boldsymbol{q}) + \dot{Q} + S_h + \dot{q}_D \tag{7}$$

In equation (7), $\dot{Q}$ and ϕ represent energy source per volume and the viscous dissipation, respectively. However, the value of viscous dissipation has been ignored in this work. S_h is the term for the conservative energy exchange from the particle phase to the fluid phase. While $\dot{q}_D$ is the enthalpy diffusion term and has been defined in equation (8). The fluid health flux is;

$$\boldsymbol{q} = -\kappa_g\nabla T_g \tag{8}$$

Where κ_g is the fluid thermal conductivity which is the sum of molecular conductivity and eddy-conductivity from Reynolds stress mixing. The enthalpy diffusion $\dot{\boldsymbol{q}}_D$ is calculated as:

$$\dot{\boldsymbol{q}}_D = \sum_{i=1}^{N_s}\nabla.(\theta_g\rho_g h_g D\nabla x_{g,i}) \tag{9}$$

The mixture enthalpy corresponds to the species enthalpies by equation (10) which C_p is defined as the mixture-specific heat at constant pressure as given by equation (11).

$$h_g = \sum_{i=1}^{N_s} x_{g,i}h_i \tag{10}$$

$$C_p = \sum_{i=1}^{N_s} x_{g,i}C_{p,i} \tag{11}$$

$C_{p,i}$ represents the specific heat of species *i*. The species are illustrated in equation (12) which $\Delta h_{g,i}$ demonstrates the heat of formation of species *i* at the reference temperature T_{ref}.

$$h_i = \int_{T_{ref}}^{T_f} C_{p,i}dT + \Delta h_{g,i} \tag{12}$$

The flow is compressible, and the equations of state can be used to determine the relationships between the gas phase pressure, enthalpy, temperature, density, and mass fractions. In CPFD, an equation of state for an ideal gas is utilized, which results in the calculation of the partial pressure of gas species as

$$p_i = \frac{\rho_g x_{g,i}RT_g}{Mw_i} \tag{13}$$

The total mean flow gas thermodynamic pressure is;

$$p = \sum_i^{N_s} p_i \tag{14}$$

where R denotes the universal gas constant, T_g denotes the temperature of the gas mixture, and Mw_i denotes the molecular weight of the gas species in question.

3.3. Discrete particle phase

The dynamics of particles is predicted by solving a transport equation for the particle distribution function (PDF), f in the MP-PIC approach [40].

$$\frac{\partial f}{\partial t} + \frac{\partial}{\partial x}(f\boldsymbol{u}_p) + \frac{\partial}{\partial \boldsymbol{u}_p}\left(f\frac{d\boldsymbol{u}_p}{dt}\right) = \frac{f_D - f}{\tau_D} \tag{15}$$

f is a function that depends on the spatial location of the particles ($\boldsymbol{x}_p$), the velocity of the particles ($\boldsymbol{u}_p$), the mass of the particles (m_p), the temperature of the particles (T_p), and the passage of time (t). Therefore, $f(\boldsymbol{x}_p, \boldsymbol{u}_p, m_p, T_p, t)d\boldsymbol{u}_p dm_p dT_P$ is the average number of particles per unit volume with velocities in the interval ($\boldsymbol{u}_p, \boldsymbol{u}_p + d\boldsymbol{u}_p$), masses in the interval ($m_p, m_p + dm_p$), and temperatures in the interval ($T_p, T_p + dT_p$). The collision damping time between particles is represented by τ_D and f_D denotes the probability density function of the mass-averaged solid velocity. The gas–solid interphase drag force, the pressure gradient, gravity, and the interaction between the solid phases all play a role in determining the particle acceleration rate [44]. The acceleration on a particle is given by,

$$\frac{\mathrm{d}\boldsymbol{u}_\mathrm{p}}{\mathrm{d}t} = D_p(\boldsymbol{u}_f - \boldsymbol{u}_p) - \frac{1}{\rho_p}\nabla p - \frac{1}{\theta_\mathrm{p}\rho_p}\nabla\tau_p + \boldsymbol{g} + \frac{\overline{\boldsymbol{u}}_p - \boldsymbol{u}_p}{\tau_D} \tag{16}$$

Here, D_p shows the drag function depending on the particle size, velocity, time, and position. θ_p is the solid volume fraction, and ρ_p represents solid density. The τ_p is the contact stress of solid depending on the spatial location. $\overline{\boldsymbol{u}}_p$ represents the local mass-averaged particle velocity. Furthermore, particle collision damping time is shown by τ_D. The solid volume fraction is given by,

$$\theta_\mathrm{p} = \iiint f\frac{m_p}{\rho_p}dm_p d\mathrm{u}_p dT_p \tag{17}$$

As can be seen, the solid volume fraction is related to the f (PDF) and the fluid volume fraction can be calculated as $\theta_f = 1 - \theta_p$.

The interphase drag coefficient is;

$$D_p = \frac{3}{8}C_d\frac{\rho_g}{\rho_p}\frac{|\boldsymbol{u}_g - \boldsymbol{u}_p|}{r_p} \tag{18}$$

The Wen and Yu drag model [45] is adopted to calculate C_d in this study

$$\mathrm{Re} < 1000 C_d = \frac{24}{\mathrm{Re}}\left(1 + 0.15\mathrm{Re}^{0.687}\right)\theta_g^{-2.65}$$

$$\mathrm{Re} \geq 1000 C_d = 0.44\theta_g^{-2.65} \tag{19}$$

$$\mathrm{Re} = \frac{2\rho_g|\boldsymbol{u}_g - \boldsymbol{u}_p|r_p}{\mu_g} \tag{20}$$

Where μ_g is the molecular gas viscosity ad the particle radius is

$$r_p = \left(\frac{3V_p}{4\pi}\right)^{1/3} \tag{21}$$

A particle's normal stress approximates neighbor particle effects. Spatial gradients are generated on the Eulerian grid and applied to discrete particles in the MP-PIC approach [40]. Gradients in this particle pressure cause particle accelerations that prohibit particle volume fractions from exceeding their close-pack limit. As the solids volume percentage approaches zero, particle pressure decreases monotonically. The particle normal stress models particle-to-particle collisions. Particle volume fraction, estimated from grid-mapped particle volumes, determines particle stress [46]. This particle normal stress model is adapted from;

$$\tau = \frac{P_p\theta_p^\beta}{\max\left[(\theta_{CP} - \theta_P), \varepsilon(1 - \theta_p)\right]} \tag{22}$$

where ε is a rather low value, on the order of 10^7, in order to remove the singularity. θ_{CP} denotes the close-packed solid volume fraction.

The conservative mass, momentum, and energy transfer between gaseous and solid phases are calculated as:

Where h_p is particle enthalpy.m_p and T_p are the mass and the temperature of the particles respectively.

$$\delta\dot{m}_p = -\iiint f\frac{dm_p}{dt}dm_p d\boldsymbol{u}_p dT_p \tag{22}$$

$$F = -\iiint f\left\{m_p\left[D_P\left(\boldsymbol{u}_g-\boldsymbol{u}_p\right)-\frac{\nabla p}{\rho_p}\right]+\boldsymbol{u}_p\frac{dm_p}{dt}\right\}dm_p d\boldsymbol{u}_p dT_p \tag{23}$$

$$S = \iiint f\left\{m_p\left[D_p\left(\boldsymbol{u}_g-\boldsymbol{u}_p\right)^2-c_v\frac{dT_p}{dt}\right]-\frac{dm_p}{dt}\left[h_p+\frac{1}{2}\left(\boldsymbol{u}_g-\boldsymbol{u}_p\right)^2\right]\right\}dm_p d\boldsymbol{u}_p dT_p \tag{24}$$

For the particle energy equation, it is assumed that the temperatures of the particles are the same throughout, that chemical reactions inside the particles do not release heat, and that chemical reactions on the surfaces of particles do not make a big difference to the surface energy balance [42]. Conductive heat transfer is ignored because it does not make a big difference [42,47]. In this work, only convective heat transfer (Q_{pg}), radiative heat transfer (Q_{radi}), and heat from a chemical reaction (ΔH_{rp}) are taken into account [47].

$$m_p c_v\frac{dT_p}{dt} = Q_{pg}+Q_{radi}-\Delta H_{rp} \tag{25}$$

$$Q_{pg} = \frac{\lambda_g Nu_{g,p}}{d_p}A_p\left(T_g-T_p\right) \tag{26}$$

$$Q_{radi} = \sigma\varepsilon_p A_p\left(T_o^4-T_p^4\right) \tag{27}$$

The variables denoted by the symbols σ, ε_p, and T_o, respectively, are the Stefan-Boltzmann constant, the emissivity of the particles, and the temperature of the surrounding environment.

3.4. Chemical reaction

Biomass gasification has four steps: drying, devolatilization (pyrolysis), heterogeneous reactions, and homogeneous reactions.

3.4.1. Drying

This entails removing any moisture that may be present in the fuel, which is subsequently vaporized after the process. The amount of pressure that is present within the reactor is a significant factor that plays a role in determining the temperature at which drying begins. For example, the temperature at which water boils can range anywhere from 373 to 550 K [5] depending on the operating pressure, which can be anywhere from 1 to 60 bars. This is because the boiling point of water is directly related to the amount of energy that is being applied to it [48].

Moist Fuel → Fuel + H_2O (g).

The biomass drying rate is described as; [49]

$$r_1 = 5.13\times10^{10}\exp\left(\frac{-10585}{T_p}\right)m_{\text{moist - bio}} \tag{R1}$$

where $m_{\text{moist - bio}}$ is the mass of biomass.

3.4.2. Pyrolysis

Pyrolysis is also known as the thermal decomposition of organic material at elevated temperatures in the absence of oxygen. It involves breaking the weak bonds between the aromatic clusters in the feedstock. This makes light gases (volatile matter) and hydrocarbons with a high molecular weight (tar) come out, and it also makes a carbonized residue. Pyrolysis is carried out at a very rapid pace thanks to the high temperatures that are maintained within the EF reactor. The compositions that are released during pyrolysis from the fuel can be described by the following equilibrium equation, and the problem of determining the yield of each product can be solved with the assistance of the elemental conservation relationships.

$$\text{Biomass} \rightarrow \alpha_1 CH_4+\alpha_2 CO_2+\alpha_3 CO+\alpha_4 H_2+\alpha_5 H_2O+\alpha_6\text{char}(s)+\alpha_7\text{ash}(s)$$
$$\sum_i \alpha_i = 1 \tag{R2}$$

Various methods can be used to calculate stoichiometric coefficients. Based on experimental results, pyrolysis products' coefficient values can be assigned [35,50,51]. The benefit of this approach is that all coefficient values are derived directly from experimental measurements. The composition of volatile matter in lignin is provided in Table 3. These results have been experimentally measured through the fast pyrolysis of lignin at a high temperature of 1073 K [35]. The proximate and ultimate analyses of biomass feedstock and pyrolysis experiments can be used to calculate the stoichiometric coefficients (α) of each component [49].

Sulfur, nitrogen, and chlorine are assumed to not participate in reactions and are passed directly to the ash. Tar is fully converted to non-condensable gases and is not included in this model. The low content of tar in product gas under a high gasifier temperature and its negligible effect on bed hydrodynamics are the reasons for this simplification [25]. The devolatilization rate is calculated using a first-order Arrhenius law [47].

$$\frac{dm_{\text{volatile}}}{dt} = -A\exp\left(-\frac{E}{RT_p}\right)m_{\text{volatile}}$$
$$A = 5.0\times10^6 s^{-1}, E = 1.2\times10^8 J/kmol \tag{28}$$

Where m_{volatile} is the mass of the volatiles left in the particle, and T_p is the temperature of the particles. The process of devolatilization is assumed to be energy neutral because the heat of devolatilization is usually very small compared to the heat of reactions that happen when char is oxidized. Due to the elevated temperatures within the EF reactor, the volatiles are rapidly released, and this release rate is computed using Equation 28. As these volatile compositions are liberated from the fuel particles, their combustion and gasification processes are inherently considered through the homogeneous reactions detailed in Table 4.

3.4.3. Char combustion and gasification

During the partial oxidation process, the volatile products and some of the char react with oxygen to produce carbon dioxide (CO_2), carbon monoxide (CO), and water (H_2O). This reaction gives heat to subsequent reactions in the gasification process. The unreacted carbon reacts with CO_2 and H_2O to produce CO, CH_4, and H_2. During gasification, there are a lot of endothermic reactions.

$$C+O_2 \rightarrow CO_2 \tag{R3}$$

$$C+CO_2 \leftrightarrow 2CO \tag{R4}$$

$$C+H_2O \leftrightarrow CO+H_2 \tag{R5}$$

$$C+2H_2 \leftrightarrow CH_4 \tag{R6}$$

3.4.4. (R3) is the partial oxidation of char (carbon) which is exothermic. The endothermic gasification reactions are shown in Table 4 including the Boudouard reaction, steam gasification, and methanation. The reaction kinetics were first suggested by Syamlal and Bissett [52], and

Table 3
Composition of Volatile Matter for lignin (vol%) [35].

CH_4	CO	CO_2	H_2
31.68	37.398	24.483	6.439

Table 4
Reactions and kinetics rates [42,47,52,53,54,55,56,23,49,57].

	Gasification reaction	Reaction kinetic rate ($molm^{-3}s^{-1}$)
Boudouard	$C(s) + CO_2 \Leftrightarrow 2CO$ $\Delta H^{\circ}_{rnx} = +172kJ/mol$	$r_{f1} = 1.272 m_s T \exp\left(\frac{-22645}{T}\right)[CO_2]$ $r_{r1} = 1.044 \times 10^{-4} m_s T^2 \exp\left(\frac{-2363}{T} - 20.92\right)[CO]^2$
Water-gas	$C(s) + H_2O \Leftrightarrow CO + H_2$ $\Delta H^{\circ}_{rnx} = +131kJ/mol$	$r_{f2} = 1.272 m_s T \exp\left(\frac{-22645}{T}\right)[H_2O]$ $r_{r2} = 1.044 \times 10^{-4} m_s T^2 \exp\left(\frac{-6319}{T} - 17.29\right)[H_2][CO]$
Methanation	$0.5C(s) + H_2 \Leftrightarrow 0.5CH_4$ $\Delta H^{\circ}_{rnx} = -75kJ/mol$	$r_{f3} = 1.368 \times 10^{-3} m_s T \exp\left(\frac{-8078}{T} - 7.087\right)[H_2]$ $r_{r3} = 0.151 m_s T^{0.5} \exp\left(\frac{-13578}{T} - 0.372\right)[CH_4]^{0.5}$
Steam Methane reforming (SMR)	$CH_4 + H_2O \Leftrightarrow CO + 3H_2$ $\Delta H^{\circ}_{rnx} = +206kJ/mol$	$r_{f4} = 3 \times 10^5 \exp\left(\frac{-15042}{T}\right)[H_2O][CH_4]$ $r_{r4} = 0.0265 \exp\left(\frac{-32900}{T}\right)[CO][H_2]^2$
Water-gas shift (WGS)	$CO + H_2O \Leftrightarrow CO_2 + H_2$ $\Delta H^{\circ}_{rnx} = -41kJ/mol$	$r_{f5} = 7.68 \times 10^{10} \exp\left(\frac{-36640}{T}\right)[H_2O][CO]^{0.5}$ $r_{r5} = 6.4 \times 10^9 \exp\left(\frac{-39260}{T}\right)[H_2]^{0.5}[CO_2]$
Combustion	$2C(s) + O_2 \rightarrow 2CO$ $\Delta H^{\circ}_{rnx} = -111kJ/mol$	$r_{f6} = 4.34 \times 10^7 \varphi_P T \exp\left(\frac{-13590}{T}\right)[O_2]$
CH_4 oxidation	$CH_4 + 2O_2 \rightarrow CO_2 + 2H_2O$ $\Delta H^{\circ}_{rnx} = -890.57kJ/mol$	$r_{f7} = 3.552 \times 10^{11} T^{-1} \exp\left(\frac{-15700}{T}\right)[O_2][CH_4]$

then Snider et al. [42] made modifications so that they could be used for modeling particle chemistry in the MP-PIC method.

3.4.4. Homogeneous reactions

A real gasification process involves the occurrence of hundreds of gas phase reactions, often known as homogenous reactions. Postulating a restricted set of reactions that characterize the key conversion rates in the reactor is a typical strategy that is utilized in the process of including complex chemistry in a computationally tractable manner. The chemistry is shown in Table 4. The rate of the reaction is given in $molm^{-3}s^{-1}$, the mass of solids per unit volume, m_s, is given in kg/m^3, the temperature, T, is given in K, and [•] means the mole concentration (g mol/m^3) of the gas species in the brackets. Instead of calculating a single forward-reverse rate, both the forward and reverse rates are added up. The reason for separating the forward and reverse reactions is to find out which reactions are more important in the gasifier.

3.5. Shrinking core model

The CPFD model for shrinking cores operates at the individual particle level, postulating that solid material within each particle reacts when exposed to a gas species [58]. The reaction rate is influenced by three key factors as shown in Fig. 4:

1. The rate of first-order reaction.
2. The transport of fluid through the non-reactive material surrounding the core.
3. The transport of fluid through the boundary layer.

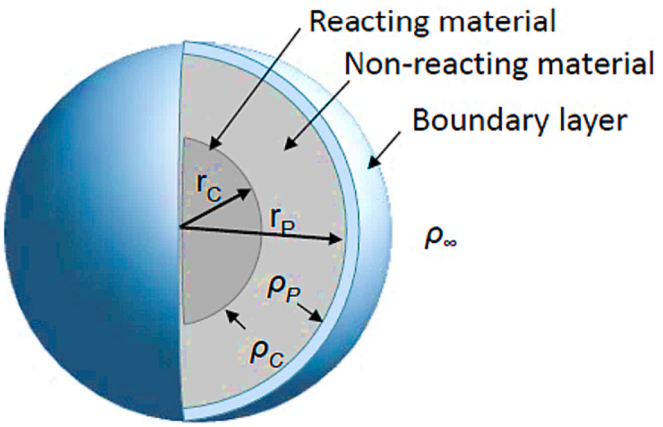

Fig. 4. Shrinking Core Reaction model diagram [58].

Every particle possesses a unique chronological record, and a 'fresh' particle will exhibit a higher degree of reaction compared to an 'old' particle. In the context of the shrinking core model, the concentration of fluid at the active core is defined by equation 29.

$$\rho_c = \frac{\rho_\infty}{k_R\left(\frac{1}{k_R} + \frac{1}{k_D} + \frac{1}{k_B}\right)} \qquad k_D = \frac{4\pi D_{m,s}}{r_p^{-1} - r_c^{-1}} \tag{29}$$

Where, ρ_c represents the fluid mass concentration at the reacting solid core (measured in kg/m^3),ρ_p is the fluid mass concentration at the particle's outer surface (measured in kg/m3), ρ_∞ denotes the fluid mass concentration in the bulk fluid (measured in kg/m^3), k_R stands for the initial reaction rate (measured in m^3/s), k_B signifies the rate of mass transfer at the boundary layer (measured in m^3/s), k_D indicates the diffusion rate through the non-reactive material (measured in m^3/s), $D_{m,s}$ represents the diffusion coefficient of the non-reacting material (measured in m^2/s), r_p corresponds to the particle's radius (measured in meters), and is the radius of the active solid core, which is calculated as follows [58]:

$$r_c = \left(\frac{3m_s}{4\pi\rho_s}\right)^{1/3} \tag{30}$$

Where m_s representing the solid material mass within the active solid core (measured in kg).ρ_s denoting the density of the solid material within the active solid core (measured in kg/m^3).

4. Simulation setup

The simulations are performed on the EF reactor at SINTEF Energy, which operates at a pressure of about 8 bars. To simplify the geometry of the EFR, illustrated in Fig. 5, the burner section of the reactor has been removed (see Fig. 8). By defining a flux plane on the entrance of the mix of nitrogen and lignin, the flow properties have been measured and used to simulate other cases.

Fig. 6 shows the mesh resolution and the boundary conditions of two different cases of the experimental tests, without the steam injection and with the installation of the steam injection tube. Biomass is fed into the reactor from the center inlet along with 60.2 NL/min of nitrogen. The initial temperature of the biomass and nitrogen is 300 K. Pure oxygen enters the reactor from the side inlet and passes through 5 small injection holes with 0.56 mm diameter. The details can be found in section 2.2. In the case of the steam injection, shown in Fig. 6c, the preheated steam enters the reactor through 14 injection holes with angles of 20° at a temperature of 700 °C.

Grid-independence and time-independence tests were performed to ensure that the numerical simulation results are not dependent on the number of grids used or the simulation time. Mesh sensitivity analysis is a crucial step in CFD simulations, as it helps to determine the appropriate mesh density required to accurately capture the flow physics of a particular problem. Based on the grid-independence test illustrated in Fig. 7, the total number of grids for the calculation domain was determined to be 3×10^5. It is important to mention that the CFD model that was employed had a limited grid resolution, which was necessary for obtaining a reasonable computational time. Highlighting the primary focus on studying particle conversion under varying gasification conditions of temperature and residence time emphasizes the importance of addressing limitations in fluid dynamics modeling. It is acknowledged that the grid resolution employed in the simulations may be insufficient for verifying intricate flow dynamics. However, these limitations, will not greatly affect the results provided in this study, as the primary focus is particle conversion under varying gasification conditions. To investigate the feasibility of auto thermal operation, a long-term simulation was performed for each case, lasting 150 s. The purpose of the simulation was to determine whether the gasifier can self-heat and maintain its temperature during a long-term operation. To exclude the start-up process, the simulation results between 80 and 150 s were taken for time-averaging.

5. Results and discussion

The results of the gas production simulations have been validated with experimental data in the following subsections. The outputs of the main gas product components (H_2, CO, CO_2, and CH_4, the dry basis of gas production without N_2) are then used to investigate the effects of various operating parameters on gasification performance. The significance of gas production in assessing the gasification process lies in its ability to account for both gas quality and fuel conversion.

5.1. Model validation

Validation is an important step in CFD modeling because it helps make sure that the simulation results are accurate and can be used to make engineering decisions. Validation can be done in several ways, such as by comparing the results of a simulation to experimental data or theoretical models or equations. In this subsection, the results of the CFD model for two different conditions, without and with steam injection have been compared with the experimental data (results in Table 2).

5.1.1. Model validation, no steam injection

In order to validate the CPFD model, the simulations have been conducted for the lignin in the boundary condition shown in Fig. 6(b) at operating conditions listed in Table 5. The experimental tests have been performed for several cases to investigate the effects of the air–fuel equivalence ratio (λ) on the gasification process because the equivalence ratio (λ) is an important parameter that affects the composition of the syngas. The ratio between the amount of oxygen in the oxidant supply and the amount required for complete stoichiometric combustion is referred to as the equivalence ratio ($\lambda = \frac{AFR}{(AFR)_{stoich}}$). When the value is close to zero it indicates pyrolysis conditions, while values equal to or greater than one indicate combustion conditions. In Fig. 8, simulation results were compared to experimental data, and the calculated values showed good agreement with the corresponding experimental measurements. When the equivalence ratio is below one ($\lambda < 1$), incomplete oxidation occurs, leading to higher levels of carbon monoxide (CO) in the syngas. As the equivalence ratio increases, the degree of oxidation increases, resulting in lower CO and H_2 levels and a higher

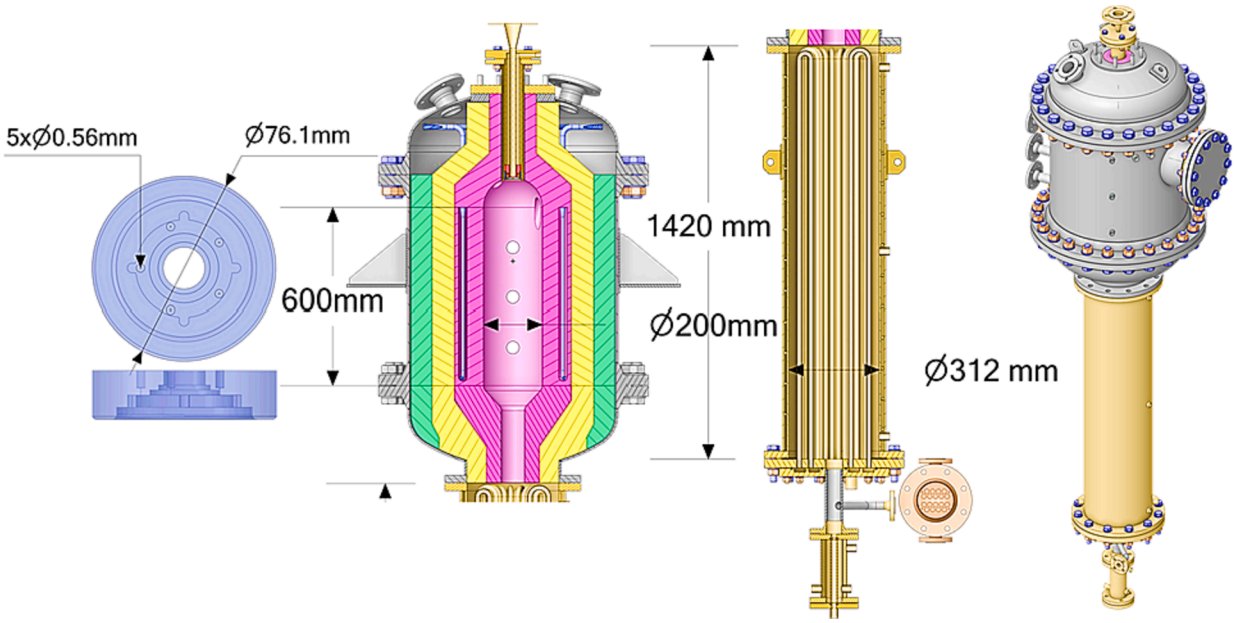

Fig. 5. The illustrations of the EFR and SolidWorks model.

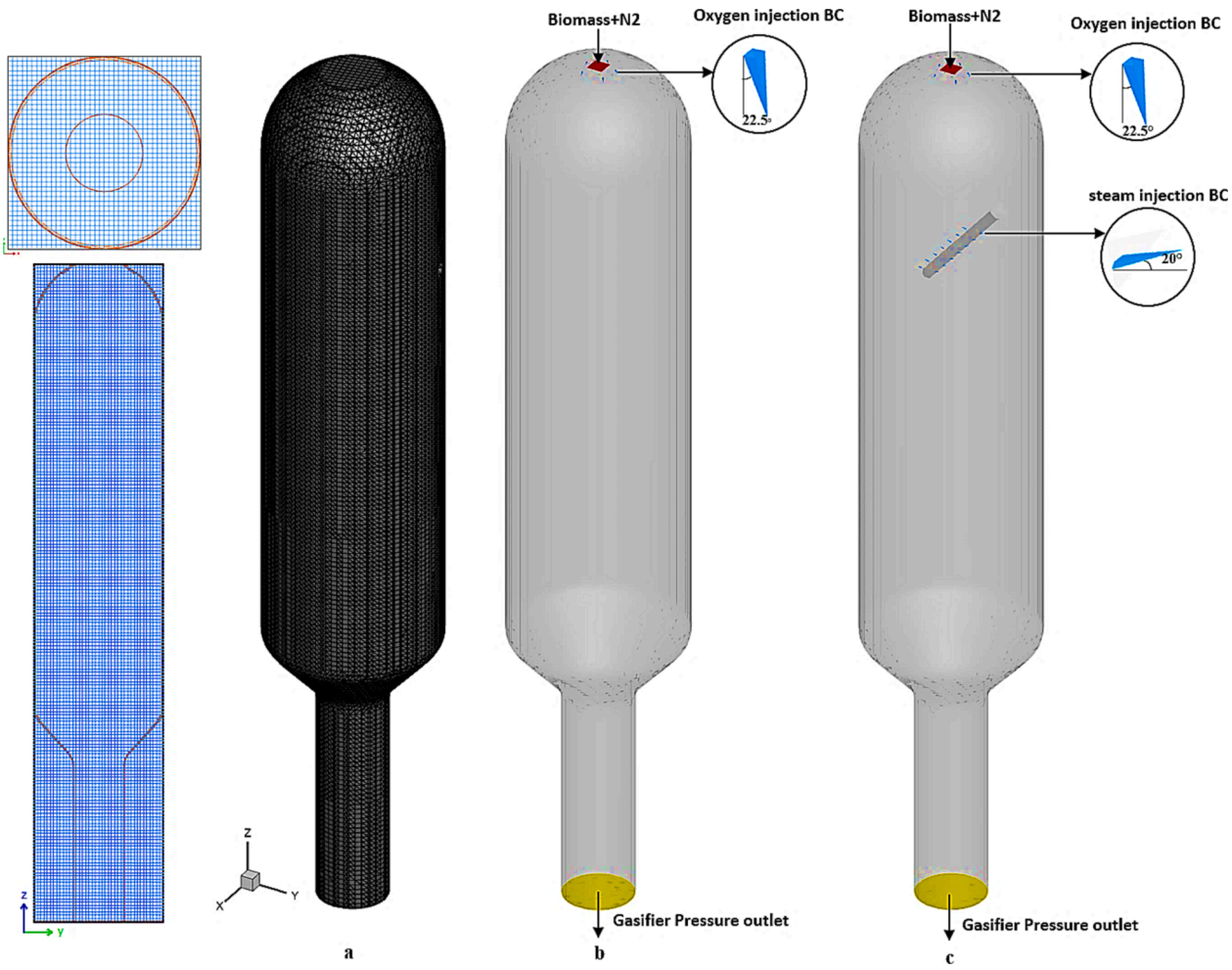

Fig. 6. A) mesh resolution, b) boundary conditions for the experimental test without the steam injection tube, and c) boundary conditions for the experimental tests with the steam injection tube.

concentration of carbon dioxide (CO_2).

The most important gasification parameter is the equivalence ratio, which affects both the stoichiometry and the CFD simulation temperature inside the gasifier as shown in Fig. 8. By increasing λ above 0.45, the combustion reactions (r_6 and r_7 in Table 4) will be promoted resulting in higher temperature and complete carbon conversion. At λ in the range of 0.4–0.5, the production of CO reached the maximum value. When λ exceeds 0.6, the temperature reaches levels greater than 2000 K, facilitating the dissociation of CO_2 and H_2O, resulting in the formation of substances such as CO, and OH (radical). In the case of H_2 and CO, the maximum relative difference is 19 % and ~ 6 %, and the minimum difference is 2.8 % and 1 % respectively. For CO_2 the relative difference falls between 1.7 % and 8.8 %. The error bars in Fig. 8 were calculated by adding the standard deviation of factors that influence the concentration measurements. These are; the variation in concentration measurements during the relevant time period, the GC deviation of the different measured compounds, variation in fuel feeding, uncertainty of flow controllers, calibration gas for the GC, and elemental composition of the feedstock.

Fig. 9 illustrates a) the particle volume fraction, b) the mole fraction of CO, and d) the fluid temperature on a plane located in the middle of the reactor. Fig. 9, c) shows the z-axis component of the fluid velocity on a plane located in the middle of the reactor. Fig. 9, e, f, g, and h show the CO_2, CO, H_2, and H_2O time averaged mole fraction at different levels in the reactor without steam injection in the operating condition of Case 3 in Table 5 at the simulation time of 150 s. In the next section, the effect of steam on the gasification process is evaluated and Fig. 9 is elaborated.

Additional significant indicators employed to evaluate the effectiveness of gasification include CCE and CGE. They are defined as [59]:

$$CCE(\%) = \frac{\dot{m}_{out,CO}\left(\frac{12}{28}\right) + \dot{m}_{out,CO_2}\left(\frac{12}{44}\right) + \dot{m}_{out,CH_4}\left(\frac{12}{16}\right)}{\dot{m}_{in,fuel}Y_C} \times 100 \quad (30)$$

where Y_C represents the mass fraction of carbon that is present in the feedstock.

$$CGE(\%) = \frac{\dot{m}_{out}(y_{H2}HHV_{H2} + y_{CO}HHV_{CO} + y_{CH4}HHV_{CH4})}{\dot{m}_{IN,Fuel}HHV_{Fuel}} \times 100 \quad (31)$$

where y_i represents the proportion of species *i* in the resultant gas, CCE is calculated based on the levels of CO_2, CO, and CH_4 in the gas product, while CGE is derived from the concentrations of H_2, CO, and CH_4. Fig. 10 illustrates the distribution of both simulation and experimental CGE and CCE versus equivalence ratio for the model without steam. The peak value for CGE (0.5) occurs at a slightly higher λ (λ = 0.45), coinciding with the complete conversion of CH_4 into other products (see Fig. 8). When λ is further increased beyond full CH_4 conversion, it leads to higher temperatures and declining CGEs due to combustion reactions (r_6 and r_7 in Table 4). Thus, by optimizing the λ value, gasification efficiency can be enhanced, leading to improved syngas quality.

5.1.2. *Model validation, with steam injection*

To examine the impact of steam on the gasification process as well as increase the reaction rate and H_2 production, steam was injected into the

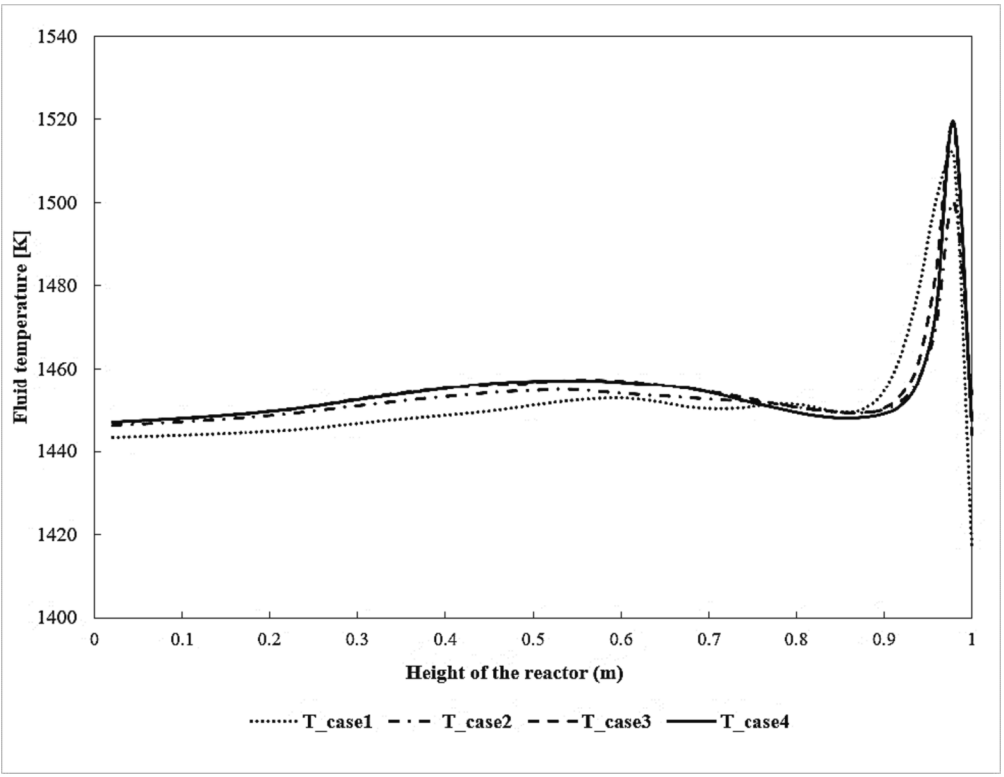

Fig. 7. Temperature distribution in the midplane in line with the height of the reactor for 4 different mesh grid sizes, the number of mesh grids for case1, case2, case3, and case 4 are 10^5, 2×10^5, 3×10^5 and 4×10^5, respectively.

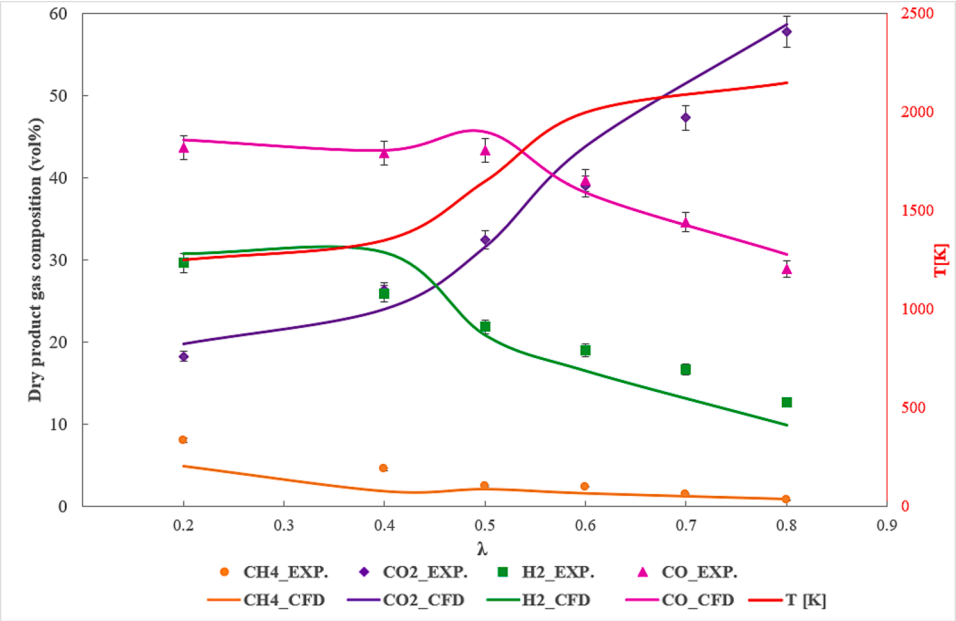

Fig. 8. Effect of equivalence ratio on dry and N_2-free product gas composition for gasification of lignin without the extra steam injection at the temperature of 1150 °C.

reactor. The steam-to-biomass ratio (S/B) is an essential parameter that has a large influence on the syngas composition. The S/B determines the amount of steam added to the gasification process relative to the amount of lignin. The simulations have been done according to four different cases (cases ST1 – ST4 in Table 6), where the S/B ratio varies from 0 to 1.5, while other operating parameters were not varied. The simulation results show a good agreement with the experimental measurement as shown in Fig. 11 for the main gas species. Similar to Fig. 8, the error bars depicted in Fig. 11 were determined by summing up the standard deviation of various factors impacting concentration measurements. These factors encompass the variability in concentration measurements over the specified time frame, the gas chromatography (GC) variance of the distinct compounds measured, fluctuations in fuel feeding, uncertainties associated with flow controllers, the calibration gas used for the GC, and

Table 5
Simulation cases without the steam injection.

Parameters	Case	S/B	λ	d¯p (μm)	fuel feeding rate (kg/h)	N2 fuel feeding (NL/min)	Pressure (bar)
equivalence ratio, λ1	Case1	0	0.2	500	2	60.21	8.26
equivalence ratio, λ2	Case2	0	0.4	500	2	60.21	8.26
equivalence ratio, λ3	Case3	0	0.5	500	2	60.21	8.26
equivalence ratio, λ4	Case4	0	0.6	500	2	60.21	8.26
equivalence ratio, λ5	Case5	0	0.8	500	2	60.21	8.26

the elemental composition of the feedstock.

In the case of H_2 and CO, the maximum relative difference is 10 % and ~ 11 %, and the minimum difference is 0.9 % and 0.02 % respectively. For CO_2 the relative difference falls within 6 % and 20 %. As the S/B increases, it is worth noting that the production of H_2 and CO_2 continues to rise while the CO yield drops linearly. These findings can mostly be attributed to a chemical mechanism known as the water–gas shift reaction (r_{f5} in Table 4), which converts CO and steam into H_2 and CO_2. Both the partial pressure of steam and its flow rate increase linearly with the S/B. This results in an increase in the rate of the water-to-gas shift reaction. Therefore, increasing the S/B ratio increases the H_2 and decreases the CO. The steam-to-biomass ratio is important since steam acts as both a reactant and a gasifying agent. If the ratio is low, the gasification process is restricted by the lack of steam, whereas if it is high, the process is limited by feedstock availability. Fig. 12 compares the CGE and CCE of the simulation and the experimental data as a function of the S/B. As can be seen from the figure, there is a good agreement between the two. Increasing the S/B tends to increase the CGE as well as CCE up to 70 % and 99 %, respectively. Therefore, when S/B is increased, it leads to higher gasification efficiency and greater production of H_2.

Fig. 13 shows the same results as in Fig. 8 but for the simulations with steam injection. In contrast to the concentration of CO_2 and H_2, the concentration of CO steadily rises along the gasifier, reaching its highest point at the outlet. By comparing Fig. 13 and Fig. 9, it can be seen that the absence of steam limits the availability of hydrogen in the gasification process (see Fig. 9), resulting in a lower hydrogen content in the product gas. The presence of steam can help reduce the concentration of carbon monoxide in the product gas, resulting in a cleaner gas composition. The syngas produced with steam addition can have a higher hydrogen-to-carbon monoxide ratio, with H_2/CO range changing from 0.4 to 0.7 (no steam injection) to 0.74–1.7 (with steam). Thus, it is more suitable for applications such as ammonia synthesis, methanol production, or hydrogen production [60]. By comparing the gasification process temperature in Fig. 9 and Fig. 13, steam resulted in the reduction of the gasification temperature. Since the steam reacts with the carbon in the feedstock, it causes an endothermic reaction, which means it consumes heat from the surrounding environment. Moreover, the evaporation of steam absorbs heat, leading to a cooling effect on the gasification temperature.

5.2. The effect of steam on the residence time

Fig. 14 depicts the particle residence time for two cases, a) no steam injection and b) with steam injection. In addition, c) shows the particle residence time distribution for both cases. The results show that the presence of steam in the reactor can affect the residence time in two ways. First, steam can increase the gas flow rate through the gasifier because of the increase in the total mass flow rate. This can reduce the residence time by carrying the solid particles through the gasifier more quickly. Furthermore, steam can promote a gasification reaction by reacting with carbon in the solid particles to form CO and H_2 and by that increase the total flow rate. At the end of the simulations, the number of particles inside the reactor for cases a and b is 3862 and 1033, respectively. In addition, the minimum residence time of particles for case a is 0.0009 s and 0.001 s for case b. The maximum residence time of particles in case a is 136.8 s and in case b, is 118.8 s.

5.3. Selection of process parameters

The operating conditions of gasification are very important for optimized performance. The effects of temperature, S/B, PSD, and λ on lignin gasification have been simulated. Table 6 lists all the operating conditions investigated.

5.4. Effect of the reactor temperature

For the simulations, the reactor temperature (Tr) was varied between 1000 °C and 1400 °C while keeping other operating parameters constant (cases T1 − T5 in Table 6). The predicted results on the gas species are shown in Fig. 15. By increasing the temperature, CO, and H_2 concentrations are enhanced. It can be explained by endothermic reactions of water–gas, Boudouard, and steam methane reforming (r_{f2}, r_{f1}, r_{f4} in Table 4). Hydrogen generation is normally favored at higher temperatures, while the production of methane is typically favored at lower temperatures. Due to lignin's complex polymer structure, high temperatures are necessary to decompose it into simpler compounds that can be converted into syngas. If the temperature is too low, the gasification will be restricted by reaction kinetics, causing an incomplete conversion. Conversely, if the temperature is too high, the reaction may be thermodynamically limited, leading to reduced yields of desired products. At higher temperatures, lignin breaks down into simpler molecules, such as phenols, aldehydes, and ketones, which react with gasifying agents such as oxygen, steam, or air to produce syngas primarily composed of CO, H_2, and CH_4 [61]. The composition and yield of syngas are also influenced by the reaction conditions, such as temperature, residence time, and λ. The yield of CH_4 was strongly affected by the process temperature. When the process temperature is above 1300 °C, the concentration of CH_4 in the syngas reaches below 1 mol% on a dry and N_2-free basis. Therefore, optimizing the gasification process temperature and other parameters can assist in achieving the desired syngas composition and yield.

5.5. Effect of the particle size

The effect of particle size on the formation of species is investigated using three different mean particle diameters (dp = 300, 500, and 700 μm; see Table 6). The effect of d¯p on the main gas composition is illustrated in Fig. 16. The projected levels of CO and H_2 decrease as d¯p gets larger; hence, smaller particle size is preferable for the generation of CO and H_2. The heat transfer, mass transfer, and reaction kinetics of the gasification process are impacted by the size of lignin particles. When the particles are smaller, reactions occur at a faster rate because of the increased surface area, which enhances the interaction between the gas and solid phase. As a result, reducing the particle size of lignin can enhance gasification efficiency, CCE, and syngas yield. Moreover, the big challenge of having fine particles lies in the energy that is needed for grinding the biomass. Furthermore, lignin particles tend to clump together, particularly at high temperatures, affecting gasification efficiency. To ensure uniform temperature and gasification, it is necessary to ensure the uniform distribution of lignin particles in the reactor. The particle size range should be optimized to achieve efficient gasification and the maximum yield of syngas while avoiding problems like clogging and erosion.

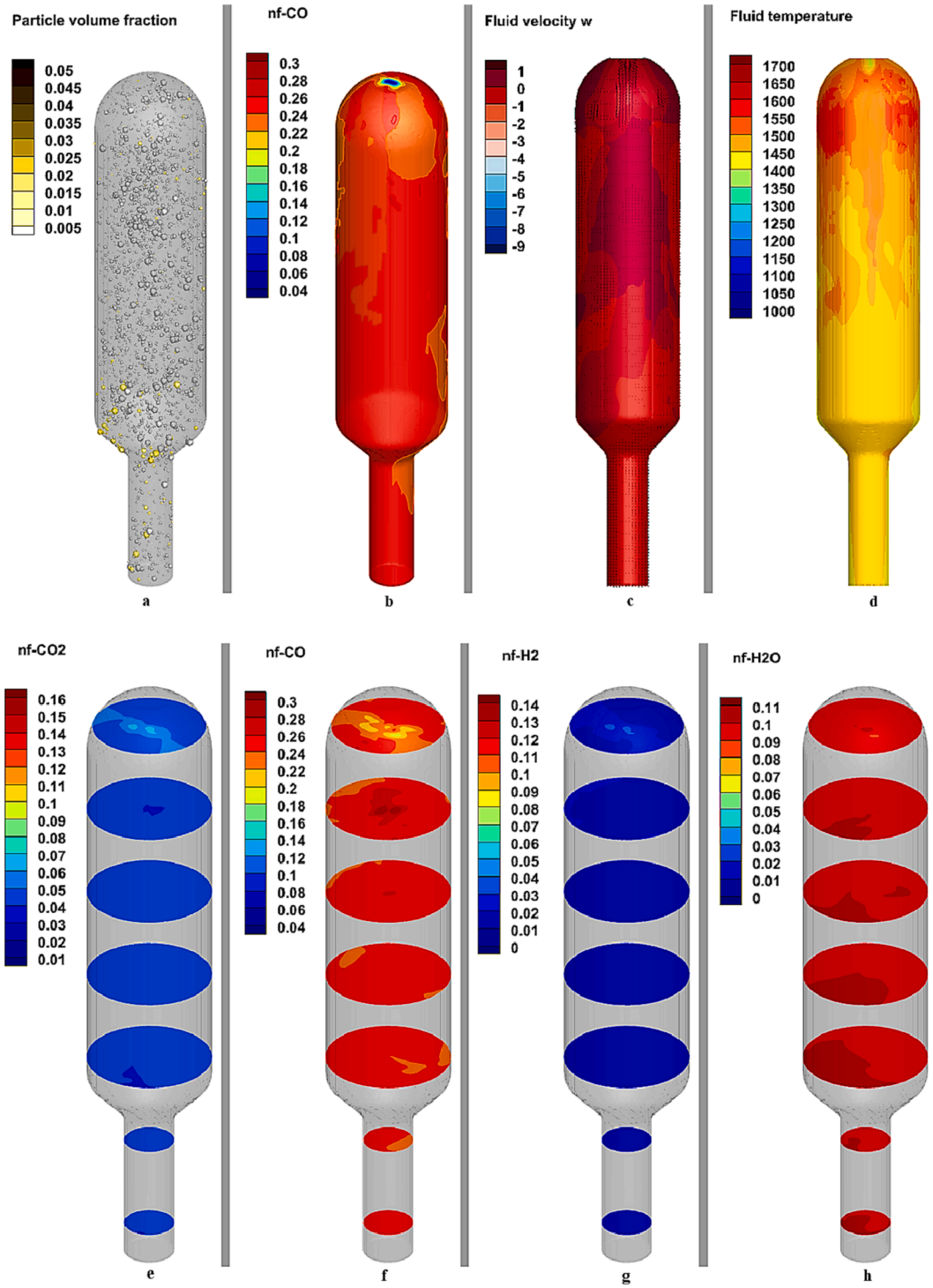

Fig. 9. Gasifier parameters as well as gas species production at levels in the reactor without the steam injection tube in the operating condition of Case 3 in Table 5, the time of simulation is 100 s.

5.6. *Effect of equivalence ratio*

The effect of the equivalence ratio on the formation of species and the conversion of carbon is investigated using nine different cases (Cases Lambda1-Lambda9; see Table 6). As can be seen in Fig. 17, an increase in λ will increase the gasification temperature due to the increased combustion of the lignin. The temperature is a critical factor because excessively high temperatures result in the formation of soot, while excessively low temperatures lead to the formation of tars. Therefore, it is essential to balance λ to ensure efficient gasification and minimize the formation of undesirable by-products. Moreover, λ affects the product gas composition, with higher λ values leading to higher yields of carbon dioxide and lower yields of hydrogen and carbon monoxideThe optimal λ value should be determined based on several factors to ensure efficient gasification and maximize the yield of syngas while minimizing the formation of undesirable by-products. Based on the findings regarding the composition of the product gas, the optimal λ for the simulated model appears to fall within the range of 0.15–0.35. Within this range, the production of H_2 and CO reaches its highest value, while the composition of CO_2 is minimized.

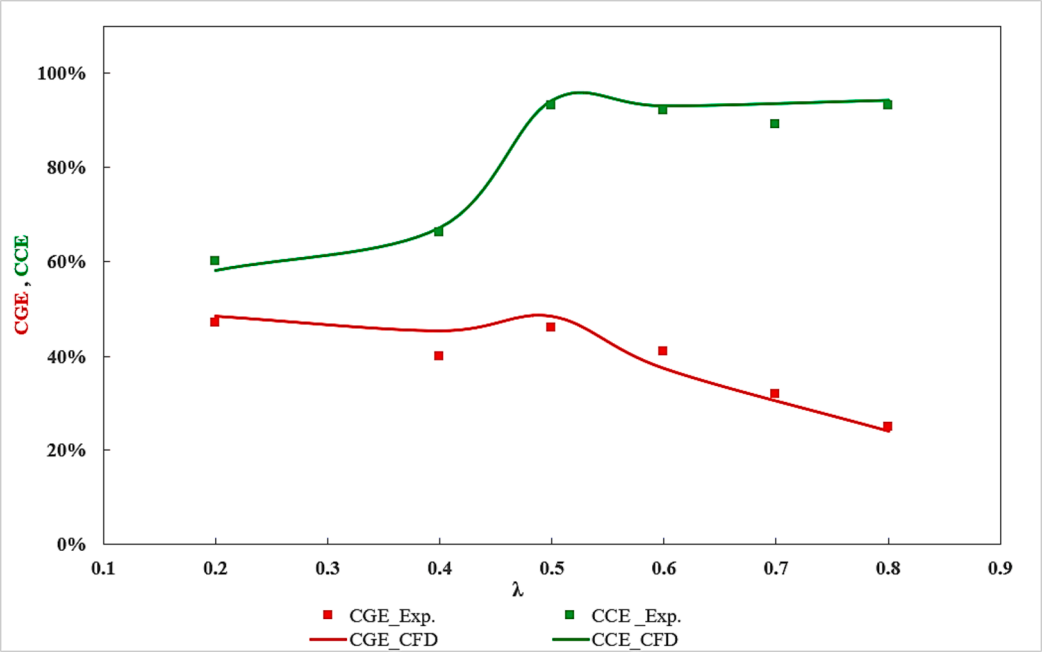

Fig. 10. Distribution of CGE and CC versus equivalence ratio for the model without steam injection.

Table 6
Parameter study cases.

Parameters	case	Fuel type	S/B	Tr (°C)	λ	$\bar{d}_p$ (μm)	fuel rate (kg/h)	N_2 feeding (NL/min)	Steam (g/min)	Pressure (bar)
reactor temperature, Tr_1	T1	lignin	1.0	1150	0.35	500	2	60.2	50	8.2
reactor temperature, Tr_2	T2	lignin	1.0	1000	0.35	500	2	60.2	50	8.2
reactor temperature, Tr_3	T3	lignin	1.0	1200	0.35	500	2	60.2	50	8.2
reactor temperature, Tr_4	T4	lignin	1.0	1300	0.35	500	2	60.2	50	8.2
reactor temperature, Tr_4	T5	lignin	1.0	1400	0.35	500	2	60.2	50	8.2
Steam1	ST1	lignin	1.0	1150	0.35	500	2	60.2	50	8.2
Steam2	ST2	lignin	0	1150	0.35	500	2	60.2	0	8.2
Steam3	ST3	lignin	0.5	1150	0.35	500	2	60.2	25.2	8.2
Steam4	ST4	lignin	1.5	1150	0.35	500	2	60.2	75.5	8.2
mean particle size(μm)	PSD1	lignin	1.0	1150	0.35	500	2	60.2	50	8.2
mean particle size(μm)	PSD2	lignin	1.0	1150	0.35	300	2	60.2	50	8.2
mean particle size(μm)	PSD3	lignin	1.0	1150	0.35	700	2	60.2	50	8.2
equivalence ratio, λ1	Lambda1	lignin	1.0	1150	0.35	500	2	60.2	50	8.2
equivalence ratio, λ2	Lambda2	lignin	1.0	1150	0.05	500	2	60.2	50	8.2
equivalence ratio, λ3	Lambda3	lignin	1.0	1150	0.15	500	2	60.2	50	8.2
equivalence ratio, λ4	Lambda4	lignin	1.0	1150	0.25	500	2	60.2	50	8.2
equivalence ratio, λ5	Lambda5	lignin	1.0	1150	0.45	500	2	60.2	50	8.2
equivalence ratio, λ6	Lambda6	lignin	1.0	1150	0.55	500	2	60.2	50	8.2
equivalence ratio, λ7	Lambda7	lignin	1.0	1150	0.65	500	2	60.2	50	8.2
equivalence ratio, λ8	Lambda8	lignin	1.0	1150	0.75	500	2	60.2	50	8.2
equivalence ratio, λ9	Lambda9	lignin	1.0	1150	0.85	500	2	60.2	50	8.2

5.7. Sensitivity analysis

Sensitivity analysis is an essential tool for understanding gasification behavior and identifying critical parameters that affect performance. It involves the systematic variation of one or more parameters and observes how this affects certain key outputs. In the gasification process, several parameters affect the process's performance, such as temperature, S/B, PSD, λ, residence time, and feedstock quality. These parameters can significantly impact the yield, composition, and quality of the product gas. Conducting sensitivity analysis helps to identify which parameters have the most impact on the process and how the process responds to changes in these parameters. This information is critical for optimizing the gasification process and achieving the desired product specifications. Sensitivity analysis can also help to identify the range of values for each parameter that provides the most efficient and effective gasification process. Moreover, sensitivity analysis can provide insights into the interactions between different parameters, which can be used to improve the process's understanding and develop new process optimization strategies [62].

The differential sensitivity analysis, which is a frequent approach that is used for this purpose, was simplified and employed in this work. The method involves calculating the derivative of the output variable for each of the input variables. The resulting values are used to determine which of the input variables has the greatest influence on the output. In differential sensitivity analysis, the sensitivity degree to which each input parameter is measured using a sensitivity coefficient. This coefficient is essentially the ratio of the change in output to the change in input when all other parameters remain constant. According to this strategy, the sensitivity coefficient, ϕ_i, with respect to the intended output Y is computed by equation (32) for a specific independent input

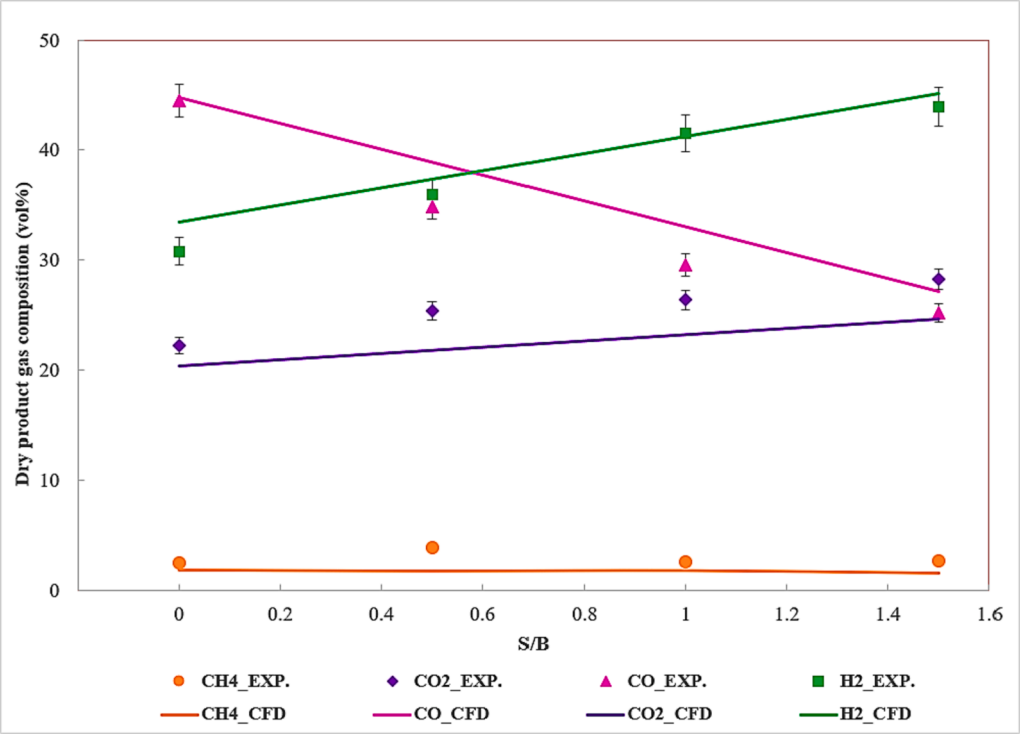

Fig. 11. Effect of steam-to-biomass ratio on dry and N_2-free product gas composition for gasification of lignin with the steam injection.

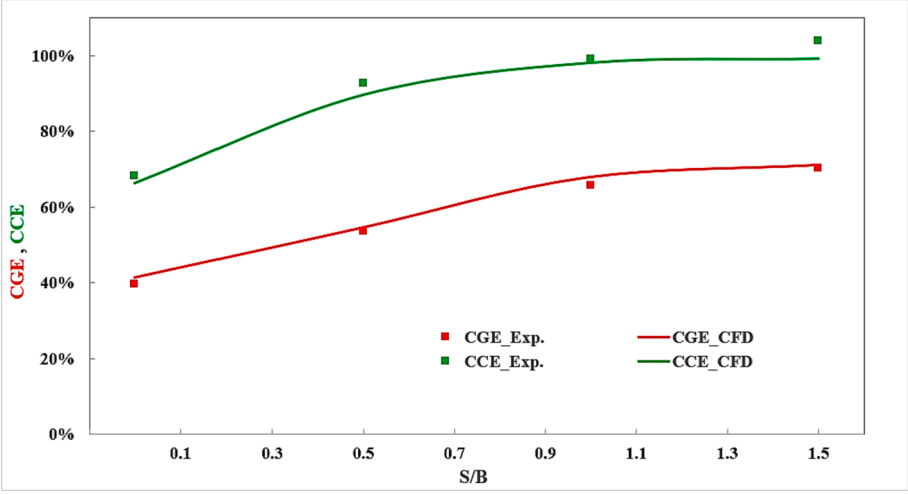

Fig. 12. The CGE and CC distribution in different steam-to-biomass ratios for the simulation and experimental results.

variable X_i, the equation states that the value ϕ_i is as follows [63]:

$$\phi_i = \frac{\partial Y}{\partial X_i}\left(\frac{X_i}{Y}\right) \tag{32}$$

where the quotient $X_{i/Y}$ is introduced to the equation in order to normalize the coefficient by eliminating the effect that the units have on the equation. By ignoring the nonlinearities, the partial derivative in equation (32) can be approximated as a finite difference for minor changes in the input parameter, and equation (32) can be reduced as follows [64]:

$$\phi_i = \frac{\%\Delta Y}{\%\Delta X_i} \tag{33}$$

Equation (33) was used to compute sensitivity analysis in this study.

In Fig. 18, the results that were computed are shown in the form of a tornado diagram. According to the findings that have been presented, the sensitivity coefficient for the temperature is high for both the production of H2 and CO. While the sensitivity coefficient of the equivalence ratio is high for the production of H2, the S/B can affect CO production more. Therefore, for the H2 production, the process parameters relative order of importance is T > λ > S/B > fuel PSD.

6. Conclusion

This paper provides a detailed description of the laboratory-scale EFR gasification results from lignin and the simulation results for selected specific operating conditions. Experiments and Eulerian-Lagrangian simulations were carried out on an oxygen-blown, steam-injected, pressurized (8.2 bars) EFR, capable of gasifying biogenic

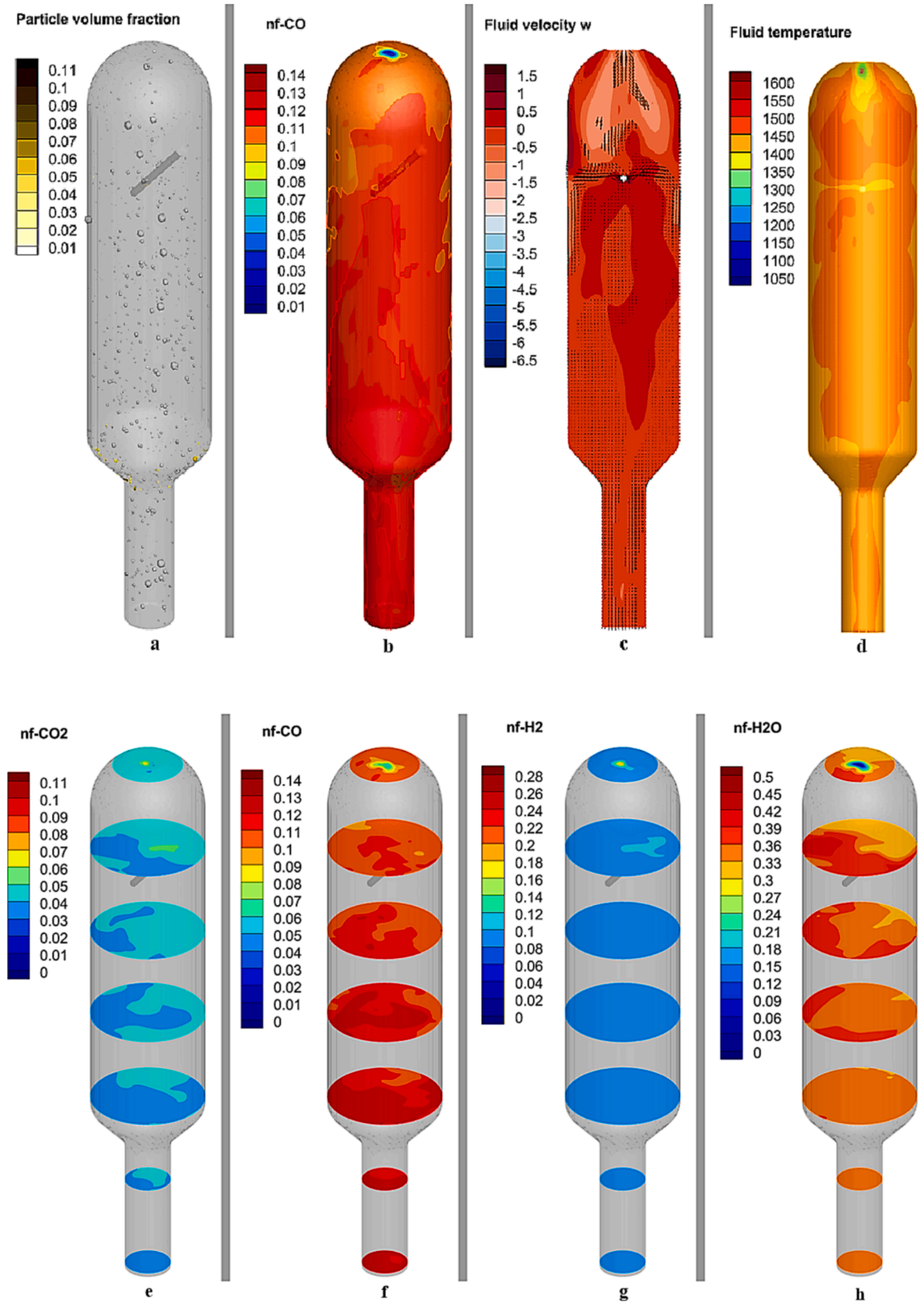

Fig. 13. Gasifier parameters as well as gas species production at levels in the reactor with the steam injection tube in the operating condition of case T1 in Table 6.

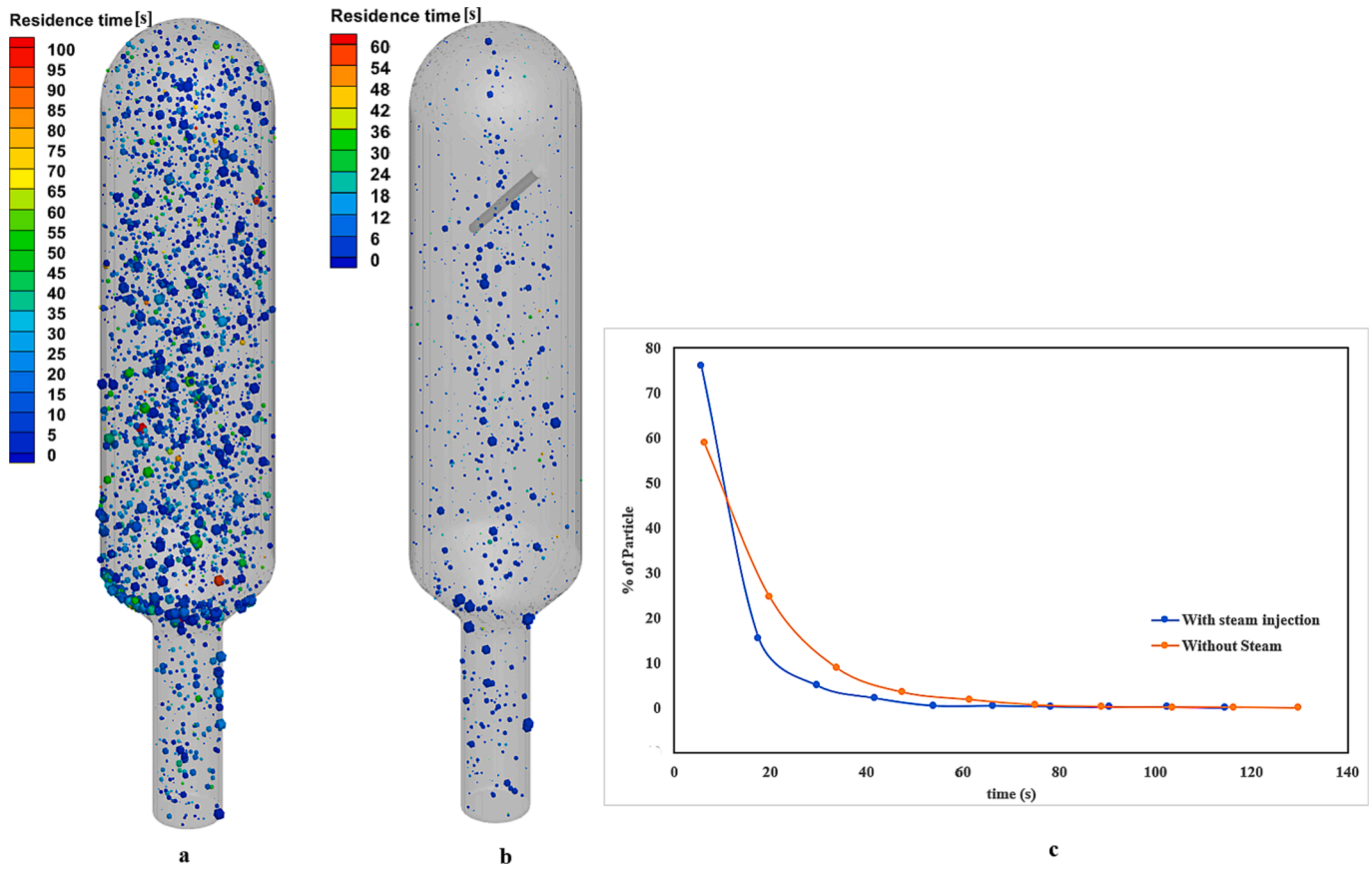

Fig. 14. Particle residence time inside the reactor based on the PSD for the lignin at the temperature of 1150 °C and λ = 0.5. a) no steam injection, b) with steam injection (S/B = 1), c) residence time distribution for both cases.

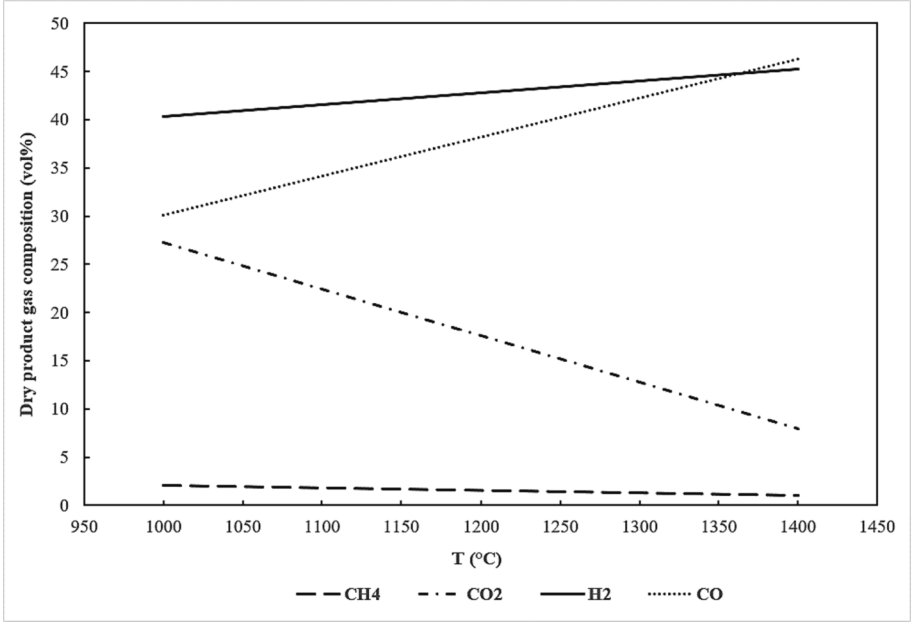

Fig. 15. The dry and N_2-free product gas composition as a function of the reactor temperature (Cases T1-T5 in Table 6).

feedstock rates ranging between 5 and 25 kW. Experimental tests were performed to study the effect of O_2 and steam on gasification efficiency. The O_2 equivalence ratio varied between 0.2 and 0.8, with no steam injection at a temperature of 1150 °C. The maximum CGE was about 47 % at a λ value of 0.5. Operating the gasifier at λ values below 0.30 resulted in a considerable decrease in CCE. Experiments with steam addition showed that for a S/B between 0.5 and 1.5, at a reactor temperature of 1150 °C, the H_2 and CO_2 increased, and the CO decreased with increased S/B. Higher S/B also resulted in increased CGE and CCE, up to 70 % and 99 %, respectively. A multiscale Eulerian-Lagrangian

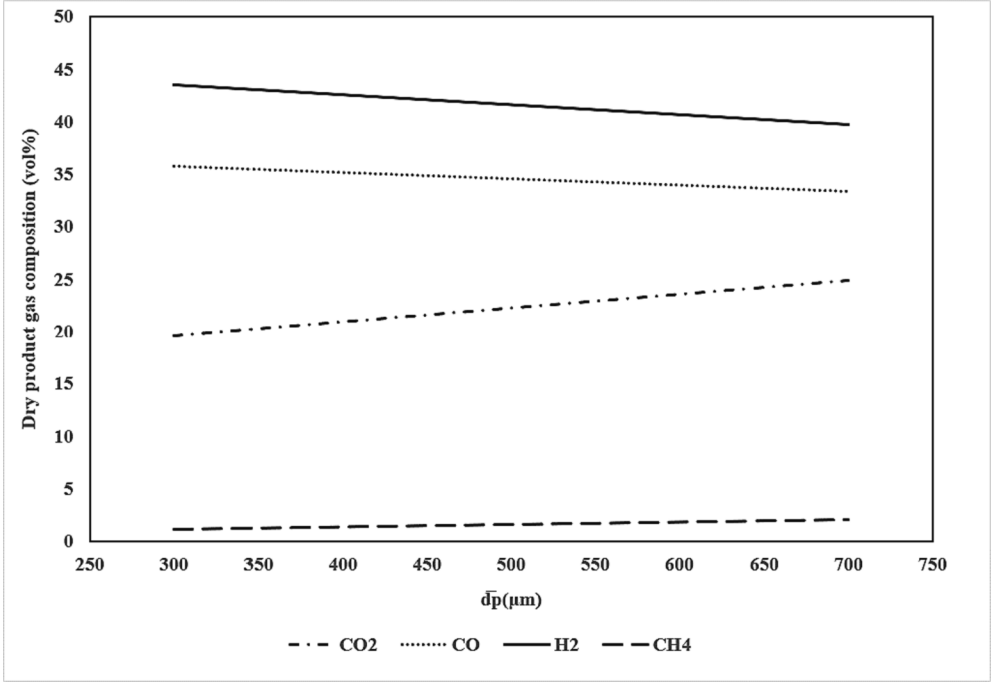

Fig. 16. The dry and N_2-free product gas composition as a function of the mean particle size (Cases PSD1-PSD3 in Table 6).

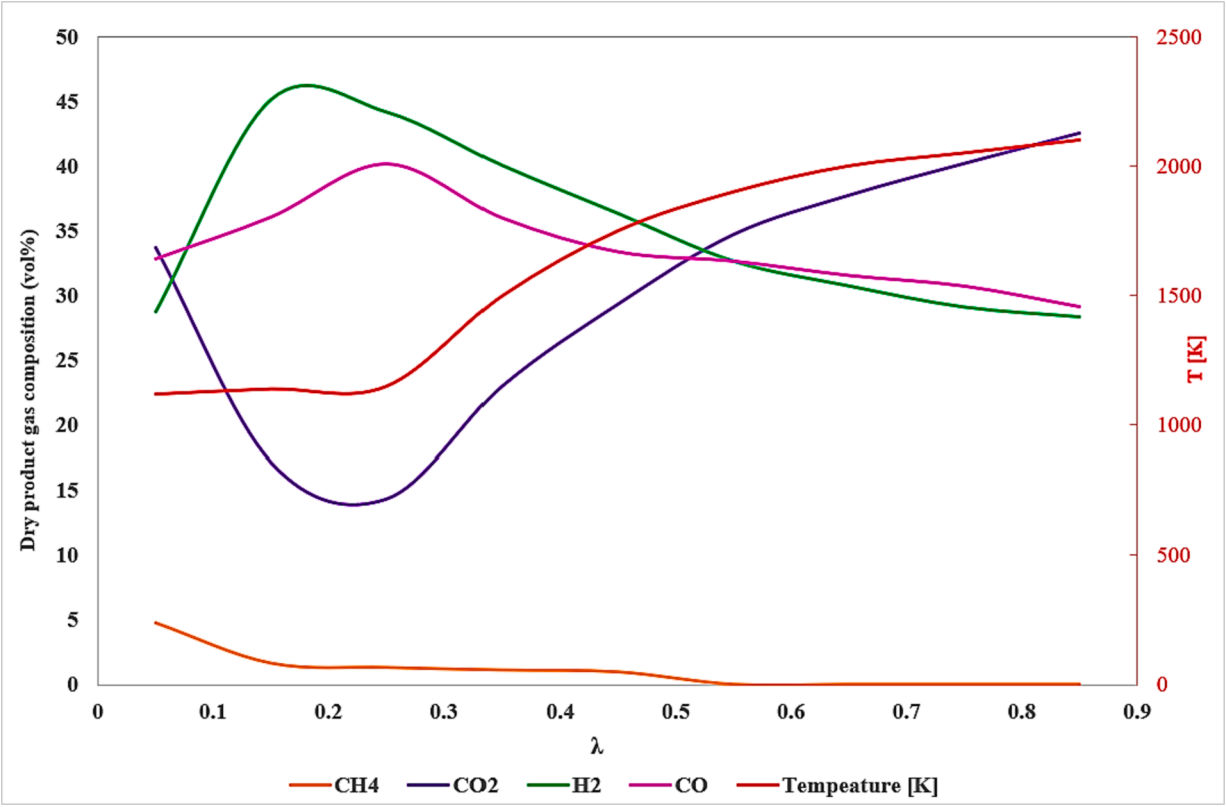

Fig. 17. The dry and N_2-free product gas composition and temperature of gasification as a function of the equivalence ratio (Lamda1-Lambda9 in Table 6).

CPFD model for EF reactor simulations has been developed and validated by experimental data. The model considers heat/mass transfer, pyrolysis, reactions, radiation, and gas-particle interactions. This model explored the effects of four key parameters: reactor temperature, S/B, λ, and PSD. Important findings were (a) Higher reactor temperatures enhanced H_2 and CO production at the cost of decreased CH_4. (b) CH_4 concentration below 1 mol% required temperature above 1300 °C. (c) Increasing λ and PSD reduced H_2 and CO production. (d) Optimal λ was in the range of 0.15–0.35. (e) Sensitivity analysis showed that temperature had a large impact on H_2 and CO production, while the S/B ratio affected CO, and λ influenced H_2.

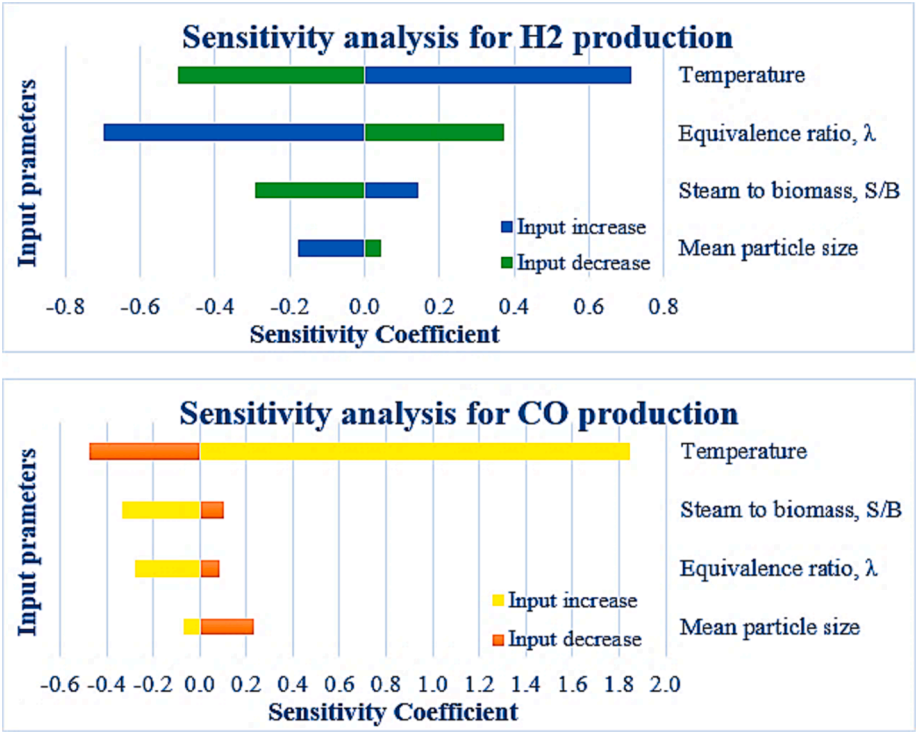

Fig. 18. Sensitivity analysis of uncertain gasification parameters.

CRediT authorship contribution statement

Nastaran Samani: Writing – original draft, Writing – review & editing, Validation, Software, Resources, Methodology, Investigation, Formal analysis, Conceptualization, Visualization, Data curation. **Roger Khalil:** Writing – original draft, Writing – review & editing, Validation, Resources, Methodology, Investigation, Formal analysis, Supervision, Project administration, Funding acquisition, Conceptualization, Visualization. **Morten Seljeskog:** Writing – original draft, Writing – review & editing, Validation, Resources, Methodology, Investigation, Formal analysis, Supervision, Project administration, Funding acquisition, Conceptualization, Visualization. **Jørn Bakken:** Data curation. **Rajan K. Thapa:** Writing – review & editing. **Marianne S. Eikeland:** Writing – review & editing, Supervision.

Declaration of competing interest

The authors declare that they have no known competing financial interests or personal relationships that could have appeared to influence the work reported in this paper.

Data availability

Data will be made available on request.

Acknowledgments

Funding: We gratefully acknowledge the financial support provided by the Bio4Fuel project, the Centres for Environment-friendly Energy Research (FME) (Project Number: 257622), the BioSynGas project, which is partly funded by the Research Council of Norway (Project Number: 319723), and the Norwegian Continental Shelf: A Driver for Climate Positive Norway, NCS C+ (Project Number: 328715).

References

[1] Mahinpey N, Gomez A. Review of gasification fundamentals and new findings: Reactors, feedstock, and kinetic studies. Chem Eng Sci 2016;148:14–31.
[2] Motta IL, Miranda NT, Maciel Filho R, Maciel MRW. Biomass gasification in fluidized beds: A review of biomass moisture content and operating pressure effects. Renew Sustain Energy Rev 2018;94:998–1023.
[3] Bergseng E, Eid T, Løken Ø, Astrup R. Harvest residue potential in Norway – A bio-economic model appraisal. Scand J For Res 2013;28:470–80. https://doi.org/10.1080/02827581.2013.766259.
[4] Ku X, Li T, Løvås T. Eulerian-Lagrangian simulation of biomass gasification behavior in a high-temperature entrained-flow reactor. Energy Fuels 2014;28:5184–96.
[5] Molino A, Chianese S, Musmarra D. Biomass gasification technology: The state of the art overview. J Energy Chem 2016;25:10–25. https://doi.org/10.1016/j.jechem.2015.11.005.
[6] Higman C, van der Burgt M, Higman C, Vanderburgt M. The thermodynamics of gasification. Gasif Amst Boston Gulf Prof PubElsevier Sci 2008:11–31.
[7] Arena U. Process and technological aspects of municipal solid waste gasification. A review Waste Manag 2012;32:625–39. https://doi.org/10.1016/j.wasman.2011.09.025.
[8] Safarian S, Unnþórsson R, Richter C. A review of biomass gasification modelling. Renew Sustain Energy Rev 2019;110:378–91.
[9] Breault RW. Gasification processes old and new: a basic review of the major technologies. Energies 2010;3:216–40.
[10] Basu P. Biomass gasification and pyrolysis: practical design and theory. Academic press; 2010.
[11] Basu P. Design of biomass gasifiers. Biomass Gasif Pyrolysis 2010:167–228.
[12] Qin K, Lin W, Jensen PA, Jensen AD. High-temperature entrained flow gasification of biomass. Fuel 2012;93:589–600.
[13] Coda B, Cieplik MK, de Wild PJ, Kiel JH. Slagging behavior of wood ash under entrained-flow gasification conditions. Energy Fuels 2007;21:3644–52.
[14] Tremel A, Stemann J, Herrmann M, Erlach B, Spliethoff H. Entrained flow gasification of biocoal from hydrothermal carbonization. Fuel 2012;102:396–403.
[15] Zhou J, Chen Q, Zhao H, Cao X, Mei Q, Luo Z, et al. Biomass-oxygen gasification in a high-temperature entrained-flow gasifier. Biotechnol Adv 2009;27:606–11.
[16] Weiland F, Hedman H, Marklund M, Wiinikka H, Öhrman O, Gebart R. Pressurized Oxygen Blown Entrained-Flow Gasification of Wood Powder. Energy Fuels 2013;27:932–41. https://doi.org/10.1021/ef301803s.
[17] Weiland F, Wiinikka H, Hedman H, Wennebro J, Pettersson E, Gebart R. Influence of process parameters on the performance of an oxygen blown entrained flow biomass gasifier. Fuel 2015;153:510–9. https://doi.org/10.1016/j.fuel.2015.03.041.
[18] Billaud J, Valin S, Peyrot M, Salvador S. Influence of H2O, CO2 and O2 addition on biomass gasification in entrained flow reactor conditions: Experiments and modelling. Fuel 2016;166:166–78.

[19] Liao L, Zheng J, Zhang Y, Li C, Yuan C. Impact of torrefaction on entrained-flow gasification of pine sawdust: an experimental investigation. Fuel 2021;289:119919.
[20] Vegendla SNP, Heynderickx GJ, Marin GB. Comparison of Eulerian-Lagrangian and Eulerian-Eulerian method for dilute gas–solid flow with side inlet. Comput Chem Eng 2011;35:1192–9. https://doi.org/10.1016/j.compchemeng.2010.09.001.
[21] Vegendla et al. - 2011 - Comparison of Eulerian–Lagrangian and Eulerian–Eul.pdf n.d.
[22] Adeyemi I, Janajreh I, Arink T, Ghenai C. Gasification behavior of coal and woody biomass: Validation and parametrical study. Appl Energy 2017;185:1007–18.
[23] Timsina R, Thapa RK, Moldestad BME, Eikeland MS. Computational particle fluid dynamics simulation of biomass gasification in an entrained flow gasifier. Chem Eng Sci X 2021;12:100112. https://doi.org/10.1016/j.cesx.2021.100112.
[24] Ku X, Wang J, Jin H, Lin J. Effects of operating conditions and reactor structure on biomass entrained-flow gasification. Renew Energy 2019;139:781–95.
[25] Abani N, Ghoniem AF. Large eddy simulations of coal gasification in an entrained flow gasifier. Fuel 2013;104:664–80.
[26] Watanabe H, Kurose R. Modeling and simulation of coal gasification on an entrained flow coal gasifier. Adv Powder Technol 2020;31:2733–41. https://doi.org/10.1016/j.apt.2020.05.002.
[27] Kumar M, Ghoniem AF. Multiphysics Simulations of Entrained Flow Gasification. Part I: Validating the Nonreacting Flow Solver and the Particle Turbulent Dispersion Model. Energy Fuels 2012;26:451–63. https://doi.org/10.1021/ef200884j.
[28] Studies on the uptake of lead and zinc by lignin obtained from black liquor – a paper industry waste material: Environmental Technology: Vol 15, No 4 n.d. https://www.tandfonline.com/doi/abs/10.1080/09593339409385438 (accessed October 29, 2023).
[29] Wang C, Xia S, Cui C, Kang S, Zheng A, Yu Z, et al. Investigation into the correlation between the chemical structure of lignin and its temperature-dependent pyrolytic product evolution. Fuel 2022;329:125215. https://doi.org/10.1016/j.fuel.2022.125215.
[30] Furusawa T, Sato T, Sugito H, Miura Y, Ishiyama Y, Sato M, et al. Hydrogen production from the gasification of lignin with nickel catalysts in supercritical water. Int J Hydrog Energy 2007;32:699–704. https://doi.org/10.1016/j.ijhydene.2006.08.001.
[31] Öhrman OGW, Weiland F, Pettersson E, Johansson A-C, Hedman H, Pedersen M. Pressurized oxygen blown entrained flow gasification of a biorefinery lignin residue. Fuel Process Technol 2013;115:130–8. https://doi.org/10.1016/j.fuproc.2013.04.009.
[32] Zhou H, Wu C, Onwudili JA, Meng A, Zhang Y, Williams PT. Polycyclic Aromatic Hydrocarbon Formation from the Pyrolysis/Gasification of Lignin at Different Reaction Conditions. Energy Fuels 2014;28:6371–9. https://doi.org/10.1021/ef5013769.
[33] Liakakou ET, Vreugdenhil BJ, Cerone N, Zimbardi F, Pinto F, André R, et al. Gasification of lignin-rich residues for the production of biofuels via syngas fermentation: Comparison of gasification technologies. Fuel 2019;251:580–92. https://doi.org/10.1016/j.fuel.2019.04.081.
[34] Lu L, Gao X, Gel A, Wiggins GM, Crowley M, Pecha B, et al. Investigating biomass composition and size effects on fast pyrolysis using global sensitivity analysis and CFD simulations. Chem Eng J 2021;421:127789. https://doi.org/10.1016/j.cej.2020.127789.
[35] Chen D, Cen K, Zhuang X, Gan Z, Zhou J, Zhang Y, et al. Insight into biomass pyrolysis mechanism based on cellulose, hemicellulose, and lignin: Evolution of volatiles and kinetics, elucidation of reaction pathways, and characterization of gas, biochar and bio-oil. Combust Flame 2022;242:112142. https://doi.org/10.1016/j.combustflame.2022.112142.
[36] Kang S, Li X, Fan J, Chang J. Hydrothermal conversion of lignin: A review. Renew Sustain Energy Rev 2013;27:546–58. https://doi.org/10.1016/j.rser.2013.07.013.
[37] Garcia AC, Cheng S, Cross JS. Lignin Gasification: Current and Future Viability. Energies 2022;15:1–17.
[38] Mastersizer 3000 - Particle Size Analyzer | Malvern Panalytical. Malvern Panalytical n.d. https://www.malvernpanalytical.com/en/products/product-range/mastersizer-range/mastersizer-3000 (accessed October 27, 2023).
[39] Khalil RA, Seljeskog M, Bakken J, Skreiberg O. Gasification of Wood Powder in a Small-scale Entrained Flow Gasifier. Chem Eng Trans 2023;99:115–20. https://doi.org/10.3303/CET2399020.
[40] Andrews MJ, O'Rourke PJ. The multiphase particle-in-cell (MP-PIC) method for dense particulate flows. Int J Multiph Flow 1996;22:379–402.
[41] Snider DM, O'Rourke PJ. The multiphase particle-in-cell (MP-PIC) method for dense particle flow. Comput. Gas-Solids Flows React. Syst. Theory Methods Pract.: IGI Global; 2011. p. 277–314.
[42] Snider DM, Clark SM, O'Rourke PJ. Eulerian-Lagrangian method for three-dimensional thermal reacting flow with application to coal gasifiers. Chem Eng Sci 2011;66:1285–95. https://doi.org/10.1016/j.ces.2010.12.042.
[43] Shui Q, Duan C, Wu X, Zhang Y, Luo X, Hong C, et al. A hybrid dynamic Smagorinsky model for large eddy simulation. Int J Heat Fluid Flow 2020;86:108698.
[44] Chen C, Werther J, Heinrich S, Qi H-Y, Hartge E-U. CPFD simulation of circulating fluidized bed risers. Powder Technol 2013;235:238–47. https://doi.org/10.1016/j.powtec.2012.10.014.
[45] Wen CY. Mechanics of fluidization 1966;62:100–11.
[46] Harris SE, Crighton DG. Solitons, solitary waves, and voidage disturbances in gas-fluidized beds. J Fluid Mech 1994;266:243–76.
[47] Zhu X, Wang Z, Ocone R, Wang H. MP-PIC simulation on CO2 gasification of biomass in a pilot plant circulating fluidized bed gasifier. Fuel 2023;332:125992.
[48] Mularski J, Pawlak-Kruczek H, Modlinski N. A review of recent studies of the CFD modelling of coal gasification in entrained flow gasifiers, covering devolatilization, gas-phase reactions, surface reactions, models and kinetics. Fuel 2020;271:117620. https://doi.org/10.1016/j.fuel.2020.117620.
[49] Liu H, Cattolica RJ, Seiser R. CFD studies on biomass gasification in a pilot-scale dual fluidized-bed system. Int J Hydrog Energy 2016;41:11974–89. https://doi.org/10.1016/j.ijhydene.2016.04.205.
[50] Debiagi PEA, Gentile G, Pelucchi M, Frassoldati A, Cuoci A, Faravelli T, et al. Detailed kinetic mechanism of gas-phase reactions of volatiles released from biomass pyrolysis. Biomass Bioenergy 2016;93:60–71. https://doi.org/10.1016/j.biombioe.2016.06.015.
[51] Detailed Chemical Kinetic Modeling of Vapor-Phase Reactions of Volatiles Derived from Fast Pyrolysis of Lignin n.d. 10.1021/acs.iecr.5b01289.
[52] Syamlal M, Bissett LA. METC Gasifier Advanced Simulation (MGAS) model. USDOE Morgantown Energy Technology Center (METC). WV (United States) 1992. https://doi.org/10.2172/10127635.
[53] Bustamante F, Enick RM, Killmeyer RP, Howard BH, Rothenberger KS, Cugini AV, et al. Uncatalyzed and wall-catalyzed forward water–gas shift reaction kinetics. AIChE J 2005;51:1440–54.
[54] Gómez-Barea A, Leckner B. Estimation of gas composition and char conversion in a fluidized bed biomass gasifier. Fuel 2013;107:419–31.
[55] Yoon H, Wei J, Denn MM. A model for moving-bed coal gasification reactors. AIChE J 1978;24:885–903.
[56] Wan Z, Hu J, Qi X. Numerical analysis of hydrodynamics and thermochemical property of biomass gasification in a pilot-scale circulating fluidized bed. Energy 2021;225:120254. https://doi.org/10.1016/j.energy.2021.120254.
[57] Gómez-Barea A, Leckner B. Modeling of biomass gasification in fluidized bed. Prog Energy Combust Sci 2010;36:444–509.
[58] CPFD Software LLC. Barracuda Virtual Reactor. Cpfd-Softw 2013. https://cpfd-software.com/wp-content/uploads/2020/10/CPFD_Barracuda_Release_Guide_16.0.pdf.
[59] Chen W-H, Chen C-J, Hung C-I, Shen C-H, Hsu H-W. A comparison of gasification phenomena among raw biomass, torrefied biomass and coal in an entrained-flow reactor. Appl Energy 2013;112:421–30.
[60] Higman C. Chapter 11 - Gasification. In: Miller BG, Tillman DA, editors. Combust. Eng. Issues Solid Fuel Syst., Burlington: Academic Press; 2008, p. 423–68. 10.1016/B978-0-12-373611-6.00011-2.
[61] Li C, Zhao X, Wang A, Huber GW, Zhang T. Catalytic Transformation of Lignin for the Production of Chemicals and Fuels. Chem Rev 2015;115:11559–624. https://doi.org/10.1021/acs.chemrev.5b00155.
[62] Hamby DM. A review of techniques for parameter sensitivity analysis of environmental models. Environ Monit Assess 1994;32:135–54.
[63] Moradi A, Samani NA, Kumara AS, Moldestad BM. Evaluating the performance of advanced wells in heavy oil reservoirs under uncertainty in permeability parameters. Energy Rep 2022;8:8605–17.
[64] Moradi A, Tavakolifaradonbe J, Moldestad BM. Data-Driven Proxy Models for Improving Advanced Well Completion Design under Uncertainty. Energies 2022;15:7484.